Study of electric and magnetic field fluctuations from Lower Hybrid Drift Instability waves in the terrestrial magnetotail with the fully kinetic, semi-implicit, adaptive Multi Level Multi Domain method

M. E. Innocenti,[1] C. Norgren,[2,3] D. Newman,[4] M. Goldman,[4] S. Markidis,[5] and G. Lapenta[1]

[1)] *Center for mathematical Plasma Astrophysics, Department of Mathematics, KULeuven (University of Leuven), Celestijnenlaan 200B, B-3001 Leuven, Belgium*

[2)] *Swedish Institute of Space Physics, Uppsala, Sweden*

[3)] *Department of Physics and Astronomy, Uppsala University, Uppsala, Sweden*

[4)] *Center for Integrated Plasma Studies, University of Colorado Boulder, Gamow Tower, Boulder, 80309-0390 Colorado, USA*

[5)] *Department of Computational Science and Technologies, KTH Royal Institute of Technology, Stockholm, Sweden*

(Dated: 28 September 2016)

The newly developed fully kinetic, semi-implicit, adaptive Multi-Level Multi-Domain (MLMD) method is used to simulate, at realistic mass ratio, the development of the Lower Hybrid Drift Instability (LHDI) in the terrestrial magnetotail over a large wavenumber range and at a low computational cost. The power spectra of the perpendicular electric field and of the fluctuations of the parallel magnetic field are studied at wavenumbers and times that allow to appreciate the onset of the electrostatic and electromagnetic Lower Hybrid Drift Instability (LHDI) branches and of the kink instability. The coupling between electric and magnetic field fluctuations observed by Norgren *et al.*[1] for high wavenumber LHDI waves in the terrestrial magnetotail is verified. In the MLMD simulations presented, a domain ("coarse grid - CG") is simulated with low resolution. A small fraction of the entire domain is then simulated with higher resolution also ("refined grid - RG") to capture smaller scale, higher frequency processes. Initially, the MLMD method is validated for LHDI simulations. MLMD simulations with different levels of grid refinement are validated against standard semi-implicit Particle In Cell simulations of domains corresponding to both the coarse and the refined grid. Precious information regarding the applicability of the MLMD method to turbulence simulations is derived. The power spectra of MLMD simulations done with different levels of refinements are then compared. They consistently show a break in the magnetic field spectra at $k_\perp d_i \sim 30$, with d_i the ion skin depth and $k_\perp$ the perpendicular wavenumber. The break is observed at early simulated times, $\Omega_{ci} t < 6$, with Ω_{ci} the ion cyclotron frequency. It is due to the initial decoupling of electric and magnetic field fluctuations at intermediate and low wavenumbers, before the development of the electromagnetic LHDI branch. Evidence of coupling between electric and magnetic field fluctuations in the wavenumber range where the fast and slow LHDI branches develop is then provided for a Cluster magnetotail crossing.

I. INTRODUCTION

The study of turbulence processes, i.e. processes where energy, injected at large scale, is distributed over a variety of temporal and spatial scales[2], may play a key role in explaining many of the problems still open in the heliophysical and astrophysical domain.

Turbulent cascade is considered a possible explanation for the so called coronal heating problem[3], where large scale convective motion below the solar photosphere results in heat at the coronal level. In this scenario, large scale Alfvèn waves are generated by magnetic flux tube interaction and eventually deposit energy at the small scales through turbulent cascade processes[4,5]. Alfvén wave mediated turbulence may be responsible for the in-situ heating of the solar wind[6], a so-called "turbulence laboratory"[7]. In recent years, the research effort has focused on identifying the processes responsible for the breaks observed, both at the ion[8–10] and at the electron[11] scales, in the turbulent spectra of the wind. Candidates are particle interaction with kinetic Alfvén waves[12], proton cyclotron damping[13], electron or ion Landau damping[14]. The connection between turbulence and magnetic reconnection[15] has been explored more recently. In the "turbulent reconnection" scenario a stochastic field component supplied by ongoing turbulent processes reduces the characteristic length scales of magnetic reconnection and increases the reconnection rate with respect to the classical Sweet-Parker result[16], thus providing a new path to fast magnetic reconnection. Turbulent environments such as the solar wind have been shown to generate small scale reconnection sites[17–20]. In 3D kinetic simulations of reconnection from non stochastic initial configurations, turbulence is produced at late times by secondary instabilities in the out-of-plane direction[21–23]. Roytershteyn *et al.*[24] study the influence of turbulence generated by the Lower Hybrid Drift Instability in magnetic reconnection.

As widespread as the impact of turbulence in space plasmas may be, the understanding of its underlying physical mechanisms is still far from complete. As it is often the case in space physics, simulations are used to supplement theoretical investigations and observations. Kinetic simulations of turbulence, in many different flavors (gyro-kinetic[25,26], hybrid[27,28], Vlasov[12], Particle In Cell - PIC[29–31]) are currently favored over fluid simulations for the possibility of reproducing from first principles the wave-particle interaction processes that may inject or remove energy from the turbulent cascade. However, a compromise has often to be reached between the level of fidelity to nature of a simulation (e.g., a reduced

mass ratio reduces the computational costs, but risks altering qualitatively the evolution of the process simulated[32]) and the range of wavenumbers simulated. This is a particularly dramatic choice if the aim of the study is to follow the evolution of the turbulent cascade from the large scale of energy injection to the small (ion or even electron) scales of energy dissipation.

In this paper, a new approach is proposed for the study of turbulence in magnetized plasmas. The aim is to reduce the computational cost of the simulations while retaining fundamental characteristics: a fully kinetic description of both ions and electrons, realistic simulation parameters and a wide range of wavelengths. The method proposed, the Multi Level Multi Domain method[33–35], is demonstrated through the simulation, at realistic mass ratio, of turbulence generated by the Lower Hybrid Drift Instability (LHDI). In the case of the LHDI, the use of high mass ratios is essential to ensure a clear separation between the electron and the ion scales[36]. The LHDI is considered a turbulence generator because it breaks macroscopic fields into smaller and smaller structures. The fluctuations in the electric and magnetic fields driven by the development of the LHDI in an antiparallel configuration similar to the one in the terrestrial magnetotail are studied over a large range of wavenumbers, at long simulated times and with a realistic mass ratio. The potentially extreme computational costs of realistic mass ratio simulations[37] are avoided since MLMD simulations are performed.

The Lower Hybrid Drift Instability is driven by diamagnetic drift in presence of a gradient in particle density or temperature[38,39]. The LHDI is unstable over a large range of wavenumbers $\mathbf{k} \cdot \mathbf{B} \sim 0$ and frequencies ω, $\Omega_{ci} < \omega \leq \Omega_{LH}$, where Ω_{ci} is the ion cyclotron frequency, $\Omega_{LH} \sim \sqrt{\Omega_{ce}\Omega_{ci}}$ is the lower hybrid frequency and Ω_{ce} is the electron cyclotron frequency. In particular, a fastest growing, mostly electrostatic LHDI branch (mode "A", Figure 13 later in the manuscript) develops at the edges of the current sheet with $k_\perp r_e \sim 1$ and growth rate $\gamma \leq \Omega_{LH}$ [40,41], where r_e is the electron gyroradius and $\perp$ is the current aligned direction perpendicular to the main magnetic field component. A slower electromagnetic branch (mode "B", Figure 14) develops in thin current sheets ($L_H/r_i \leq 1$, with r_i the ion gyroradius and L_H the half thickness of the Harris current sheet[42]) at the center of the current sheet and with $k_\perp \sqrt{r_i r_e} \sim 1$ and $\gamma \sim \Omega_{ci}$[36]. Kinking instabilities (mode "C", Figure 15) with longer wavelengths $k_\perp d_i = 0.5 \rightarrow 2$ and slower growth rates (fractions of Ω_{ci}) then follow[43–50]. The modification of the LHDI in presence of a large range of guide fields is addressed in Wang *et al.*[51] with a gyrokinetic electron, kinetic ion approach that allows to retain realistic ion

to electron mass ratios. In the present paper, no guide field is used.

The LHDI (and, in particular, its electromagnetic branch located deeper into the current sheet) has been studied at length for its possible role in generating anomalous resistivity in collisionless magnetic reconnection[43,47,52–55]. Anomalous resistivity acts as the "normal" resistivity produced by particle-particle collisions but is generated by non-collisional processes such as wave-particle interactions[15,56]. Another possible scenario relating the LHDI and magnetic reconnection has also received attention. The LHDI alters the thickness of the reconnection current sheet and results in anisotropic electron heating. This enhances the collisionless tearing mode and a more rapid onset of magnetic reconnection may ensue[48,57]. The LHDI has also a relevant impact in the evolution of the reconnection jet fronts[58] and may contribute to the heating and acceleration of particles in the solar corona[59].

Fluctuations of LHDI origin ("LHDI turbulence") have been observed in reconnecting current sheets in both astrophysical (e.g., Shinohara *et al.*[60], Øieroset *et al.*[61], Cattell *et al.*[62], Zhou *et al.*[63], in the terrestrial magnetotail; Cattell *et al.*[64], Bale, Mozer, and Phan[65], Vaivads *et al.*[66], in the terrestrial magnetopause) and laboratory[67] plasmas. Norgren *et al.*[1] has observed that LHDI waves couple electric and magnetic field fluctuations in the terrestrial magnetotail. This process will be investigated at depth in this paper.

The paper is organized as follows. The Multi Level Multi Domain method is briefly described in Section II. In Section III, MLMD simulations of the LHDI instability are validated (Section III A). "Mixed grid" power spectra, obtained by seamlessly joining coarse and refined grid data, are analyzed in Section III B. The increase in time of the slopes of the electric and magnetic field spectra is observed, a consequence of the development of electromagnetic LHDI branch and of electromagnetic kinking instabilities. The coupling between the fluctuations of the perpendicular electric field $\mathbf{E}_\perp$ and of the magnetic field $\mathbf{B}$ observed by Norgren *et al.*[1] for LHDI waves in the terrestrial magnetotail is observed since the beginning of the simulation in the high wavenumber range at which the electrostatic LHDI branch develops. At lower wavenumbers, $k_\perp d_i < 30$, where d_i is the ion skin depth, the coupling is observed only after the development of the electromagnetic LHDI and kinking instabilities. This introduces a break in the magnetic field fluctuation spectra at $k_\perp d_i \sim 30$ at times $\Omega_{ci} t < 6$, where Ω_{ci} is the ion cyclotron frequency. In Section III C, it is elaborated further on the role of the electron perpendicular current in coupling the electric and magnetic field fluctuations. The different spatial scales of the fluctuations in the electron and ion current are

shown. Section IV then provides evidence of coupling between electric and magnetic field fluctuations over a large wavenumber range in a Cluster[68] magnetotail crossing. Conclusions are drawn in Section V.

Additionally, in Appendix A, single level simulations of LHDI are discussed to remark on an issue that, to our current understanding, affects PIC simulations: the presence of a cut-off wavenumber, dependent on the spatial resolution, above which numerical artefacts are introduced in the field spectra. Franci *et al.*[69] is referred for a study of the influence of the number of particles and of the spatial resolution in hybrid turbulence simulations. The presence of such cut-off wavenumber constitutes a further incentive towards the use of the MLMD method in turbulence simulations.

II. THE MULTI LEVEL MULTI DOMAIN METHOD AND ITS APPLICATION TO TURBULENCE SIMULATIONS

The Multi-Level Multi-Domain (MLMD) method is a way of reducing the computational cost of fully kinetic PIC simulations by simulating at increasingly higher spatial and temporal resolutions increasingly smaller fractions of the domain. In this regards, it is similar in concept to Adaptive Mesh Refinement methods for PIC codes[70,71]. The computational cost becomes the main limiting factor to what simulations can achieve in cases, such as Innocenti *et al.*[72], where the aim is to study kinetic processes at large temporal (hundreds of inverse ion cyclotron fequency) and spatial (hundreds of ion skin depth) scales. Figure 1 illustrates a two-level MLMD system, similar to the ones used in Section III of the present study. The entire domain is simulated with a coarse grid (CG) where low resolution, usually of the order of fractions of the ion skin depth d_i, is used. A smaller part of the total domain is then simulated with a refined grid (RG), where the resolution is higher, usually of the order of fractions of the electron skin depth d_e. Different time steps are used on the different levels to fit the temporal evolution of the processes of interest and also to satisfy the stability requirements of the Implicit Moment Method (IMM)[73] algorithm used, which relates the spatial (dx) and temporal (dt) resolution as in

$$\sigma < v_{th,e} dt/dx < 1. \tag{1}$$

$v_{th,e}$ is the average electron thermal velocity and $\sigma \sim 0.01$.

The jumps in spatial and temporal resolution between the levels are indicated as Refinement

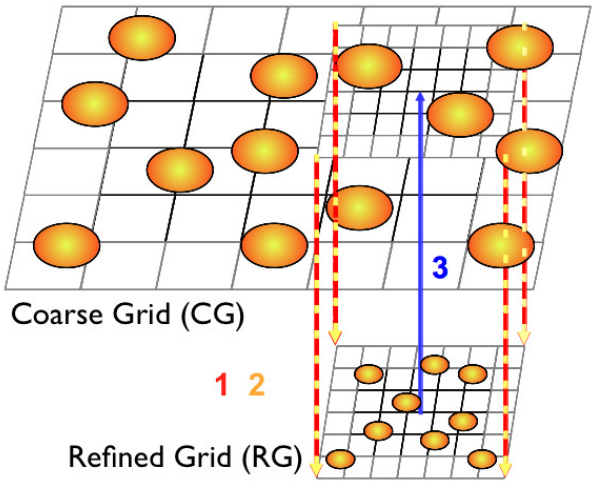

FIG. 1. Sketch of a two-level MLMD system. The Coarse Grid (CG) sends to the Refined Grid (RG) boundary conditions for fields (1- red arrow) and particles (2- yellow arrow). The higher resolution electric field is then projected to the Coarse Grid (3- blue arrow).

Factor, $RF = \Delta x/\delta x$, and Time Ratio, $TR = \Delta t/\delta t$, where Δ and δ label the resolution on the coarse and refined grid. Refinement Factors and Time Ratios as high as $RF = 14$ and $TR = 10$ have been used in Innocenti *et al.*[35]. The refined grid in a two level MLMD system has a spatial extension $L_x/RF \times L_y/RF$, with L_x and L_y the dimensions of the coarse grid. The same number of cells is currently used at all grid levels. This limitation will be removed in next versions of the code.

To maintain consistency between the different levels simulated, information regarding both fields and particles is regularly exchanged between the coarse and the refined grid: field (red arrow in Figure 1) and particle (yellow arrow) boundary conditions are exchanged from the coarse to the refined grid. The electric field calculated on the refined grid is then used in the generation of the coarse grid electric field solution for better level interlocking (blue arrow). Straightforward applications of the method are cases where it is possible, at least as a first approximation, to identify a relatively small area where processes happen at smaller temporal and spatial scales, like the Electron Diffusion Region (EDR) in magnetic reconnection simulations[74]. The MLMD method is demonstrated for magnetic reconnection applications in Beck *et al.*[34] and Innocenti *et al.*[35]. In both cases, electron scale features (the inversion layer in the Hall field[75] and the electron jets moving out of the EDR at electron Alfvén speed[76–78] respectively) are captured by the RG only at a computational cost dramatically

lower than the one of a comparable single level simulation. Figure 10 in Innocenti *et al.*[35] shows that a magnetic reconnection simulation done with the MLMD method and a jump in spatial resolution $RF = 14$ costs approximatively 70 times less than a comparable "traditional" PIC simulation. The salient features of the simulation are retained by the MLMD system at a cost which is almost two order of magnitude lower than that of a standard simulation.

A second field of applicability for the MLMD method is demonstrated in this paper. It is constituted by problems where multiple scales coexist over a domain which needs to be simulated at large scales to provide realistic injection conditions or to simulate low wavenumber fluctuations also. A small, representative portion of the domain is then simulated at higher resolution to capture the high frequency, high wavenumber dynamics.

III. ANALYSIS OF MLMD SIMULATIONS OF TURBULENCE GENERATED BY THE LOWER HYBRID DRIFT INSTABILITY

In this Section, MLMD simulations of turbulence generated by the Lower Hybrid Drift Instability are investigated.

All the simulations in this paper share the same physical initial conditions, a double Harris equilibrium[42]. The use of this configuration as initial condition is supported by observations of an Harris-like profile in the magnetopause in correspondence of observations of LHDI fluctuations[65]. A realistic mass ratio between the ions (i) and electrons (e), $m_r = m_i/m_e = 1836$, is used, the half width of the Harris current sheet is $L_H/d_i = 0.53$, the electron thermal velocity is $v_{th,e}/c = 0.045$, where c is the speed of light, and the ratio between the ion and electron temperature is $T_i/T_e = 20$. The thermal velocity $v_{th,s}$ of the generic particle species s is related to the temperature T_s as $v_{th,s} = \sqrt{k_B T_s/m_s}$, with k_B the Boltzmann constant. With this initial parameters, the ion gyroradius is $r_i/d_i = 0.69$, the Alfvén speed is $V_A/c = 0.0068$, with c the speed of light, and the ion and electron betas are $\beta_i = 0.95$ and $\beta_e = 0.048$ respectively. The asymptotic magnetic field value and the density at the centre of the current sheet have been used in the calculations of the betas. No guide field is added. The initial density of the drifting electron (species 0) and ion (species 1) populations is indicated as n_0. A background electron (species 2) and ion (species 3) population is also added, with initial density $n_b/n_0 = 0.1$. These parameters are compatible with the plasma conditions in the

magnetotail.

2D3V simulations are performed. Only the xy plane is simulated, but all the velocity and field components are retained. The x direction is aligned with the Harris current and the gradients of the Harris equilibrium are in the y direction.

Periodic boundary conditions are used for both fields and particles on the Coarse Grids. MLMD simulations with Refinement Factors $RF = 4$, $RF = 6$ and $RF = 8$ are shown.

Table I shows the simulation parameters. Lengths and cell numbers are the same in the x and y direction. The maximum wave number simulated is $k_{max} = \frac{\pi}{dx}$. $k_{sup} = k_{max}/4$ is the wavenumber at which grid effects start affecting the power spectra of the different quantities, as discussed in Appendix A. For this reasons, all the spectra shown in this paper will be represented with dotted lines at wavenumber larger than k_{sup}, to signify that that part of the spectra is affected by numerical artefacts and cannot be used for physical investigation.

All coarse grids, CG, are simulated in all three cases with domain sizes $L_{x,CG}/d_i \times L_{y,CG}/d_i = 60 \times 60$. $n_{x,CG} = n_{y,CG} = 768$ cells are used per direction, with a spatial resolution of $\Delta x_{CG} = \Delta y_{CG} = 0.079\ d_i = 3.35\ d_e$, with d_e the electron skin depth. The time step is $\omega_{pi}\Delta t_{CG} = 0.1$, with ω_{pi} the ion plasma frequency. 196 particles per species per cell are used. The same number of cells and of particles per cell is used on the Refined Grids, RGs. Hence, the number of refined grid particles sitting in the area corresponding to a coarse grid cell is $196 \times RF^2$ per species, with $RF = 4, 6, 8$. The refined grids of the three different MLMD simulations all share the same time step, $\delta t = 0.05$, with $TR = 2$ with respect to the coarse grids. The refined grids are simulated in correspondence of the upper of the two current sheets initialized and have center at $x/d_i = 30$, $y/d_i = 45$ in CG coordinates.

Table II shows the duration (second column) and the number of cores used (third column) for the MLMD simulations with different RFs. In the last row, the duration of a single grid (SG) simulation with the same parameters as the MLMD coarse grid is shown. These simulations were run on the SuperMUC machine, based in Germany at Leibniz Supercomputing Centre. The website of the Centre[79] is referred for further information on the cluster.

The duration of the MLMD simulations does not change significantly with the refinement factor, since the initial number of particles is the same in all simulations, notwithstanding the RF. The single grid simulation has approximately the same duration as the MLMD ones, but 512 rather than 2048 cores are used, making it four time cheaper. The reason is that half the number of particles and half the number of cycles are used in the single grid

	L_x (d_i)	dx (d_i)	k_{max} (d_i^{-1})	k_{sup} (d_i^{-1})
CG	60	0.0781	40.2124	10.0531
RG, $RF = 4$	15	0.0195	160.8495	40.2124
RG, $RF = 6$	10	0.0130	241.2743	60.3186
RG, $RF = 8$	7.5	0.0098	321.6991	80.4248

TABLE I. Domain size (L_x), spatial resolution (dx), nominal higher wavenumber k_{max} and upper wavenumber limit k_{sup} for the coarse (CG) and for the refined (RG) grids of the MLMD simulations. Lengths and resolutions are the same in the x and y direction.

	duration (hrs)	# of cores	ω_{pi}dt
MLMD, $RF = 4$	11.6	2048	0.05
MLMD, $RF = 6$	12.3	2046	0.05
MLMD, $RF = 8$	12.9	2048	0.05
SG, CG equivalent	11.8	512	0.1

TABLE II. Duration in hours (second column), number of cores used (third), time step normalised to the ion plasma frequency ω_{pi} (fourth) of the MLMD simulations with $RF = 4$, $RF = 6$ and $RF = 8$ analysed in the paper and of a single grid (SG) simulation with parameters corresponding to the MLMD coarse grid.

case with respect to the MLMD simulations. This single grid case aims at reproducing the Coarse Grid results alone (hence, half the number of particles than in the MLMD cases), where the time step is double with respect to the MLMD refined grids.

A. Validation of the Multi-Level Multi-Domain simulations

This paper heavily relies on previous validation efforts: a) previous validation of the MLMD method for the simulation of kinetic instabilities and b) validation of the Implicit Moment Method (IMM) and of its capability of correctly simulating the development of the Lower Hybrid Drift Instability.

Validation against theory of the growth rate of some kinetic instabilities in a MLMD system is shown in Innocenti *et al.*[33]. In Innocenti *et al.*[35] the speed of electron jets in the Re-

fined Grid of the MLMD system is validated against theoretical expectations. In Innocenti *et al.*[80], momentum conservation in the MLMD system is examined.

The Implicit Moment Method has been used to simulate the evolution of the Lower Hybrid Drift Instability in a large number of published works, among which Lapenta and Brackbill[48], Ricci *et al.*[81,82]. In Ricci *et al.*[81,82] IMM simulations of LHDI are validated against the explicit PIC code NPIC and against theory. Lapenta and Brackbill[48] proves a very important point that pushes towards the use of the MLMD method for instabilities developing over a large range of wavenumbers. It shows that a small IMM simulation with appropriate resolution correctly captures the evolution of the small-wavelength LHDI branch. In particular, the wavenumber which is expected to dominate form theory has growth rate which satisfactorily matches the theoretical expectation. Long wavelengths oscillations do not develop due to the reduced size of the box. The same paper then shows that a large box simulated with reduced resolution cannot resolve the small wavelengths so accurately but can instead represent long wavelength modes. We can then expect that grids simulated with dimensions and resolution comparable to those of MLMD Refined and Coarse Grids but independently (meaning, not part of a MLMD system and hence not subject to inter-grid communication operations) will correctly simulate the small and large wavelength LHDI ranges respectively. We still need to prove in this paper that the Refined Grid is correctly driven by the Coarse Grid in its low wavenumber range and that no artefacts are introduced as a result of grid coupling.

As a preliminary check on the outcome of the simulations, Figure 2 shows the energy evolution as a function of time on the Refined Grids. Panel (a) and (d), (b) and (e), (c) and (f) refer to the $RF = 4$, $RF = 6$ and $RF = 8$ cases. In panels (a) to (c), the energy values are normalised with respect to the initial total energy $\epsilon_{TOT,0}$. In panels (d) to (f), the normalisation is done with respect to the initial value of each energy component. The red line is the total energy, the green, blue and black lines are the energy stored in the magnetic field, in particles and in the electric field respectively. The kinetic energy is then broken into the contribution of the four particle populations: electrons (cyan) and ions (magenta), streaming (solid line) or background (dashed line). Panel (a) to (c) show that, the higher the Refinement Factor, the lower the weight of the magnetic field energy is on the total energy budget, since the refined grid is more "focused" on the current sheet than in the cases with lower RF. All three panels show that the energy is remarkably well conserved ($\epsilon_{TOT}/\epsilon_{TOT,0} = 0.9957$

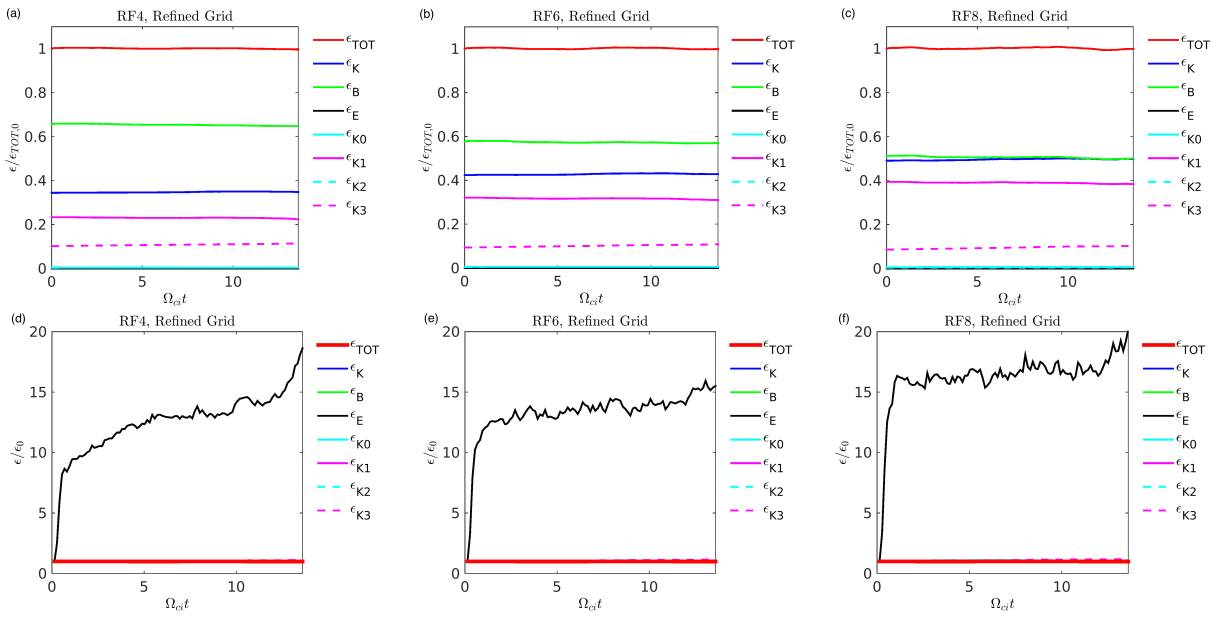

FIG. 2. Temporal evolution of the energy normalized to the initial total energy $\epsilon_{TOT,0}$ (panel a to c) and to the initial energy of each component (panel d to f) for the refined grids of the MLMD simulations and $RF = 4$ (left panels), $RF = 6$ (centre panels) and $RF = 8$ (right panels). The red line is the total energy, ϵ_{TOT}, the green, blue and black lines are the energy stored in the magnetic field, ϵ_B, in particles , ϵ_K, and in the electric field, ϵ_E. The cyan lines are the electron energies, ϵ_{K0} and ϵ_{K2}, the magenta lines the ion energies, ϵ_{K1} and ϵ_{K3}. Solid and shaded lines are used for streaming (species 0 and 1) and background (species 2 and 3) particles respectively.

for $RF = 4$, $\epsilon_{TOT}/\epsilon_{TOT,0} = 0.9986$ for $RF = 6$ and $\epsilon_{TOT}/\epsilon_{TOT,0} = 0.9985$ for $RF = 8$ at $\Omega_{ci}t = 13.6$) in all the three refined grids. This is because, contrarily for example to the magnetic reconnection example shown in Figure 6(b) in Innocenti *et al.*[35], particles are flowing in and out of the refined grids at an approximately constant rate. Panels (d) to (f) show the variation with time of each energy component. The increase in time of the energy stored in the electric field dwarfs all other variations: the electric field is initialised to zero in the entire domain, but the electric field component of the LHDI starts growing very soon once the simulation is started. The energy gained by the electric field is provided by the drifting ions, which lose energy with time.

Figure 3 and Figure 4 show the B_z field component (panel a and b) and the electron density ρ_e (panel c and d), normalized to code units, at times $\Omega_{ci}t = 5.44$ and $\Omega_{ci}t = 13.6$. Panel a and c shows a zoom of the coarse grid field at $25.25 < x/d_i < 34.75$, $42 < y/d_i < 48$.

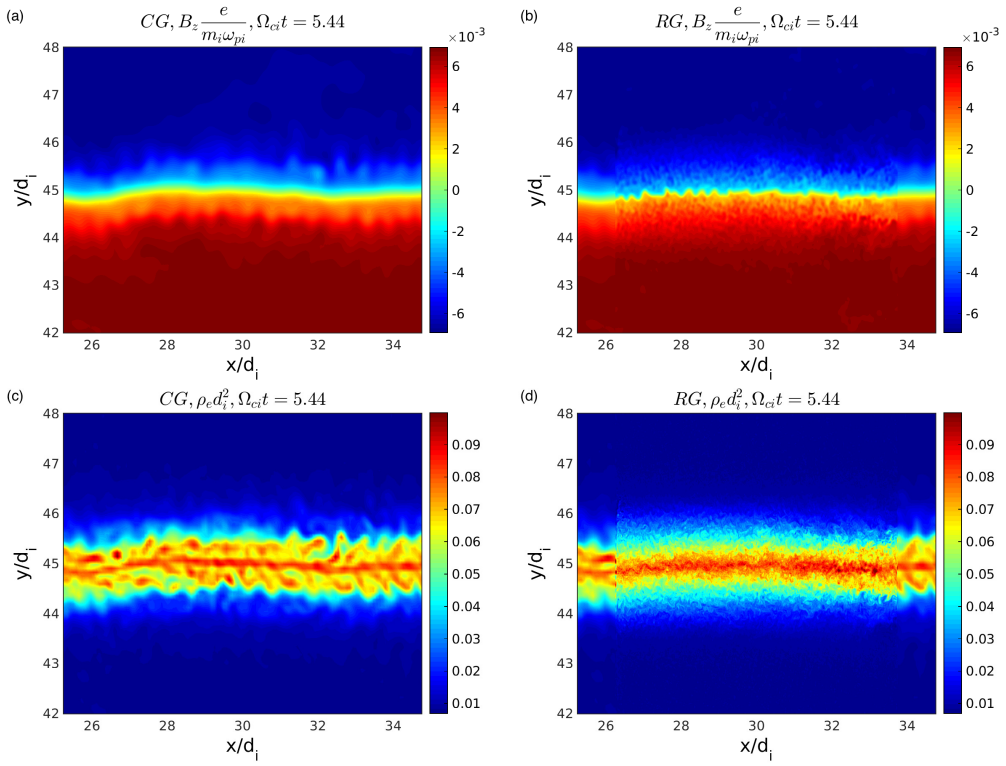

FIG. 3. B_z (panel a and b) and electron density ρ_e (panel c and d) for the MLMD simulation with $RF = 8$ and at time $\Omega_{ci} t = 5.44$. In panel a and c, the coarse grid solution in the region $25.25 < x/d_i < 34.75$, $42 < y/d_i < 48$ is shown. In panel b and d, the refined grid fields are superimposed at $26.36 < x/d_i < 33.75$, $41.25 < y/d_i < 48.75$.

In the second column, the refined grid solution is superimposed at $26.36 < x/d_i < 33.75$, $41.25 < y/d_i < 48.75$. In both Figure 3 and Figure 4, the simulation with $RF = 8$ is shown. The fastest mostly electrostatic LHDI branch has growth rate $\gamma \leq \Omega_{LH}$. The asymptotic field from the Harris equilibrium is $B_0 = 0.0068$, i.e. $\Omega_{LH}/\omega_{pi} = 0.29$ or, equivalently, $\Omega_{LH}/\Omega_{ci} = \sqrt{m_r} \sim \sqrt{1836}$. Therefore, the expected time scale for the development of the fast LHDI branch is of the order of $T\Omega_{ci} \geq 0.1466$. The electromagnetic LHDI branch, with $\gamma \sim \Omega_{ci}$, develops at time scales $T\Omega_{ci} \sim 6$. Kinking modes, whose growth rate is a fraction of Ω_{ci}, are slower. These order of magnitude expectations are confirmed in the simulations.

The coarse and refined grid solution connect, almost seamlessly, in all cases. A visual inspection reveals that the refined grid is driven by the coarse grid in the simulation of the lower wavelengths: when the coarse grid kinks macroscopically, as in Figure 4, the refined grid follows. The refined grid solution diverges instead from the coarse grid at smaller scales,

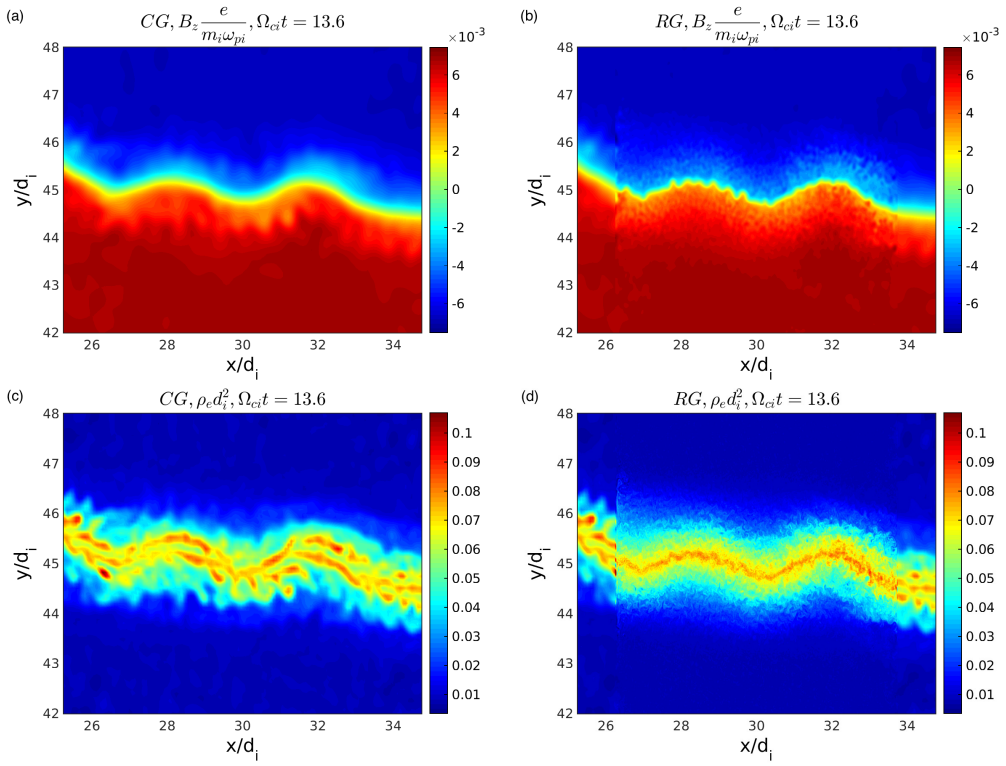

FIG. 4. B_z (panel a and b) and electron density ρ_e (panel c and d)for the MLMD simulation with $RF = 8$ and at time $\Omega_{ci} t = 13.6$. In panel a and c, the coarse grid solution in the region $25.25 < x/d_i < 34.75$, $42 < y/d_i < 48$ is shown. In panel b and d, the refined grid fields are superimposed at $26.36 < x/d_i < 33.75$, $41.25 < y/d_i < 48.75$.

since the refined grid captures high wavelength fluctuations that the other grid averages out, due to the reduced spatial resolution. In the case of the electron density in the coarse grid at time $\Omega_{ci} t = 5.44$, Figure 3, a central high density spine seems to be sided by high density branches. In Figure 4, first column, second row, the side branches are so elongated to seem able to support a bifurcated current, a process often associated to the late stages of the LHDI. However, inspection of the electron current plots in the coarse and refined grid does not show evidence of current bifurcation. In fact, the thickness of the current sheet simulated is rather low, $L_H/d_i = 0.53$, while current bifurcation is usually associated with thicker current sheets[57,82]. The electron density refined grid plots show that the coarse grid side branches are broken, at higher resolution, in smaller scale fluctuations, while the higher density central spine remains.

Kinking of the current sheet is visible in Figure 4. Long wavenumber ($k_{CD} L_H \sim 0.5 \rightarrow 2$)

kinking of an LHDI unstable current sheet is routinely observed. It has been attributed to a multitude of modes: drift kink instability, due to the relative drift between ions and electrons (Ozaki *et al.*[43], Horiuchi and Sato[47], with $k_{CD}L_H \sim 2$, Pritchett, Coroniti, and Decyk[44], with $k_{CD}L_H \sim 1$), Kelvin Helmholtz instability, driven by the ion velocity shear produced by the LHDI (Lapenta and Brackbill[48], with $k_{CD}L_H \sim 0.5$), ion-ion kink instability, where the drifts is between two ion species (i.e., drifting ion and background), rather than through electrons and ions (Karimabadi *et al.*[49,50] $k_{CD}L_H \sim 1$). CD stands here for "current direction", x in the simulations. The identification of the instability causing the kink in our current sheet is not a priority of this paper, which focuses instead on how the Refined Grid is driven to these long wavelengths by the Coarse Grid.

Lapenta and Brackbill[48] shows that, in semi-implicit simulations of the LHDI, a large domain simulation with low resolution correctly reproduces the evolution of the low wavenumber modes. Higher wavenumber modes are approximated within the resolution used. Conversely, increasingly smaller but better resolved simulations lose the ability of resolving kink modes. While commenting Figure 4, it is claimed that, in a MLMD system, the CG can drive the RG in simulating large scale modes that the RG would not be able to simulate independently. This claim is corroborated by Figure 5, which compares the power spectra of δB_z (upper cluster of lines) and E_x (lower) at time $\Omega_{ci}t = 2.72$ (panel a and c) and $\Omega_{ci}t = 8.16$ (panel b and d) for different simulations. The variations in the out of plane magnetic field, δB_z, are obtained as $\delta B_z = B_z - B_{z,init}$, where $B_{z,init}$ is the field at the initial time step. Contrarily to Innocenti and Lapenta[55], but following, for example, Daughton[36], the kinking of the neutral line has not been taken into account in the calculation. The spectra shown are cuts at an angle $\theta = 45°$ of the 2D spectra in the $k_x d_i$ vs. $k_y d_i$ plane. As such, they are shown as function of a "perpendicular wavenumber" $k_\perp$.

In Figure 5, panel a and b, the Coarse Grid solutions of the MLMD simulations with $RF = 4$ (red line), $RF = 6$ (black) and $RF = 8$ (green) are contrasted with a standard PIC simulation done with the same parameters as the CGs, the "Sm 5" simulations from Appendix A. In panel c and d, the Refined Grids of the MLMD simulations with $RF = 4$ (red line), $RF = 6$ (black) and $RF = 8$ (green) are contrasted with a standard PIC simulation ("RG comp", blue line) done with the same parameters of the RG of the $RF = 4$ case. The focus at the moment is on the low wavenumber range, defined here as $k_\perp d_i < 2$. Remind that, as previously remarked, the part of the spectra plotted with dotted lines is

affected by numerical artefacts and should not be considered for analysis. The power at low wavenumber tends to increase with time, as a result of the development of high wavelength modes (see also the Appendix). This is visible comparing panel a and c with b and d, especially for the δB_z field. In panel a, one sees that the CG solutions and the CG comparison simulation overlap very well at $\Omega_{ci}t = 2.72$. In panel c, instead, again at $\Omega_{ci}t = 2.72$, the "RG comp" simulation reaches significant lower power levels than the Refined Grids in the low wavenumber range. This behaviour is constant in time. In panel d, for example, where $\Omega_{ci}t = 8.16$, the RG results superimpose among themselves at power levels which are evidently driven by the CG solution (compare panel d and c; more on CG/RG result superposition will follow in the next Section). The comparison simulation (blue line, "RG comp") is evidently not able to simulate large wavelength mode and rests at lower power level in the lower wavenumber range. This proves that CG/RG coupling drives the RGs into the simulation of low wavenumber modes that the single grids alone would not be able to reproduce, a major result for the CG/RG coupled system.
After showing the driving effect of the Coarse Grids on the Refined Grids, it is now possible to focus on the coupled CG/RG system.

Figure 6 shows, in each panel, the δB_z and E_x power spectra for the coarse (red and green lines) and refined (blue and black lines) grids at time $\Omega_{ci}t = 2.72$.
The three panels refer to the MLMD simulations with $RF = 4$ (panel a), $RF = 6$ (panel b) and $RF = 8$ (panel c). The upper limit of the horizontal axis is the highest wavenumber simulated by the refined grid in the $RF = 8$ case, $k_\perp d_i = 321.7$.

The horizontal axes of Figure 6 allow to appreciate at a glance the strength of the MLMD approach. The simulation with $RF = 8$ extends of a factor eight the available range of wave numbers with respect to the coarse grids, at a minimum computing cost with respect to the simulation of the CG alone (see Table II). To reach the same upper wavenumber with a single level 2D simulation, an increase of computing cost of a factor $RF^2 = 64$ has to be expected.
Figure 6 provides empirical proof that the spectra changes at $k_\perp > k_{sup}$ (where spectra are plotted with dotted lines) are not of physical origin, but numerical artefacts related to the local spatial resolution. In all the cases, the same pattern is present in all the grids: a variation in the slope of the spectra of δB_z is accompanied by the appearance of a plateaux in the spectra of E_x. These very similar structures are pushed at different wavenumbers,

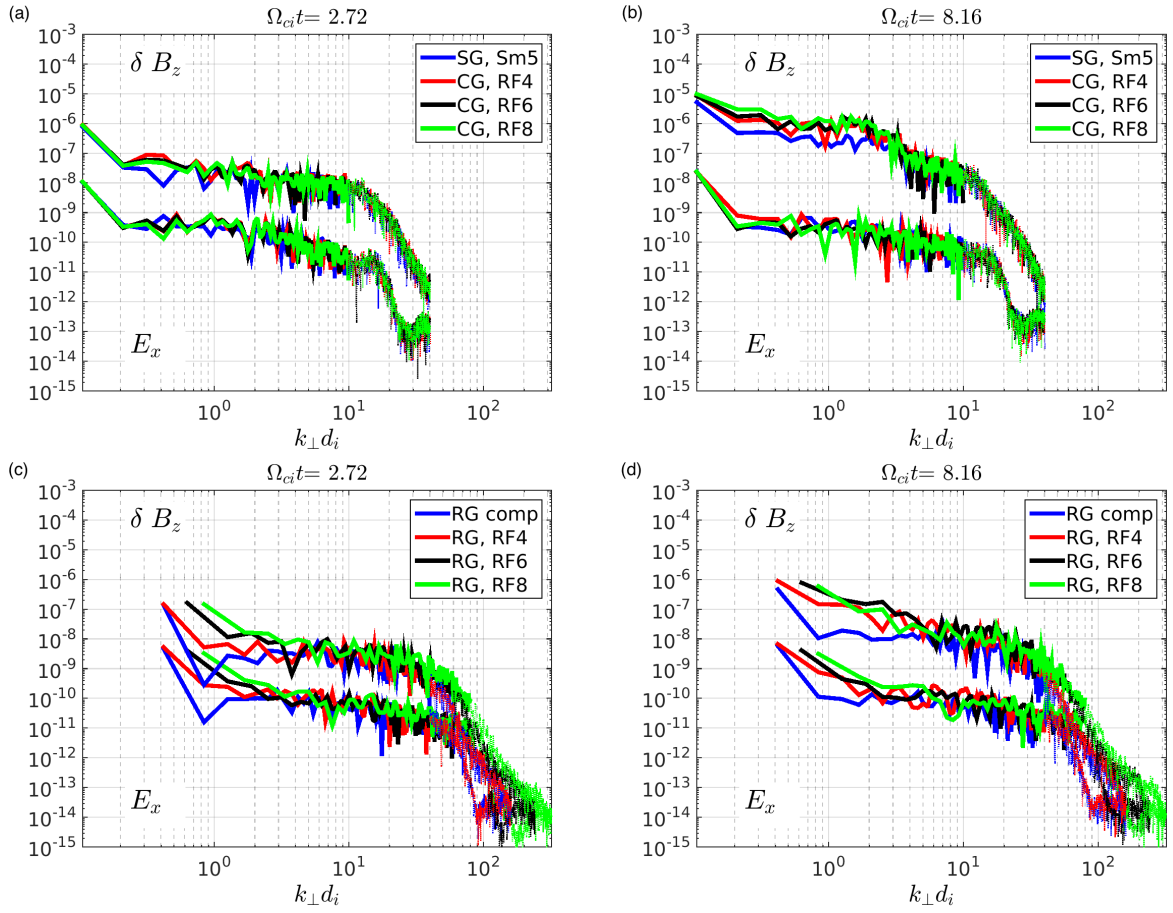

FIG. 5. Numerical power spectra of the fluctuations of the B_z (δB_z, upper four upper lines) and of the E_x (four lower lines) field components as a function of $k_\perp$ at time $\Omega_{ci}t = 2.72$ (panel a and c) and $\Omega_{ci}t = 8.16$ (panel b and d). In panel a and b, the Coarse Grids of the MLMD simulations with $RF = 4$ (red), $RF = 6$ (black), $RF = 8$ (green) are contrasted with a single level simulation with the same parameters as the CGs (blue, "SG, Sm5"). In panel c and d, the Refined Grids of the MLMD simulations with $RF = 4$ (red), $RF = 6$ (black), $RF = 8$ (green) are contrasted with a single level simulation with the same parameters as the RG in the $RF = 4$ simulation (blue, "RG comp"). The dotted lines mark the wavenumber ranges, $k_\perp > k_{max}/4$, which are deemed unreliable for physical investigations.

according to the local resolution, on the Coarse and Refined Grids. The fact that, discarding the red and green dotted lines, the coarse and refined grid spectra connect seamlessly, for both δB_z and E_x, at all the RF represented, constitutes further proof in the same direction. Since approximately the last quarter of the entire wavenumber range simulated by a grid

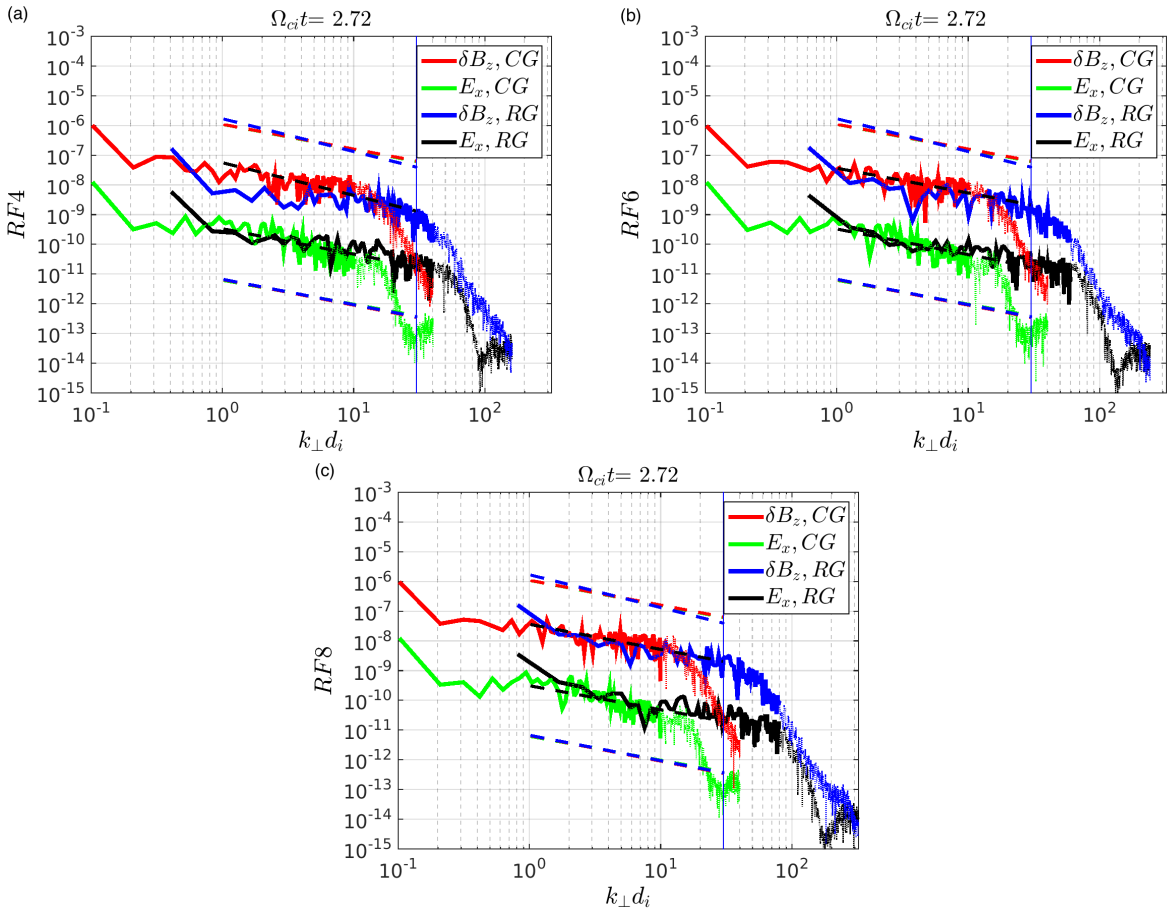

FIG. 6. Numerical power spectra of the fluctuations of the B_z (δB_z) and of the E_x field components as a function of $k_\perp$ at time $\Omega_{ci}t = 2.72$ for the MLMD simulations with $RF = 4$ (panel a), $RF = 6$ (panel b) and $RF = 8$ (panel c). The red and green lines identify the coarse grid B_z and E_x power spectra, the blue and black lines the refined grid δB_z and E_x power spectra. The dotted lines mark the wavenumber ranges, $k_\perp > k_{max}/4$, which are deemed unreliable for physical investigations. The slopes calculated from the mixed grid spectra for the B_z (E_x) fields are shown above (below) the spectra in the three panels in blue ($RF = 4$), red ($RF = 6$) and green ($RF = 8$) respectively. The dashed black lines superimposing the δB_z and E_x mixed grid spectra in each panel are the fit calculated for that particular RF. The blue vertical line marks $k_\perp d_i = 30$.

is unavailable for physical investigation, it is even more important to have cheap methods, such as the MLMD method, to extend the range of "reliable" wavenumbers of a system. The MLMD system permits to build a "mixed level" spectrum, composed by coarse grid points at the "reliable" CG wavenumbers, $k_\perp d_i < k_{sup,CG}$, and by refined grid points beyond

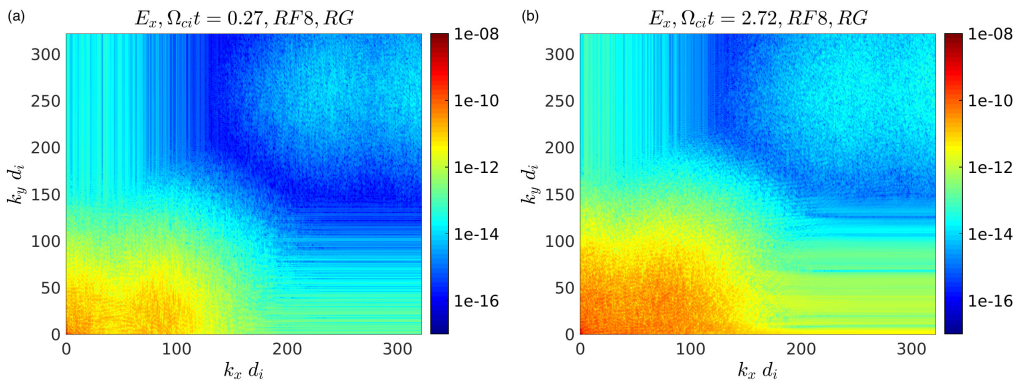

FIG. 7. Numerical power spectra of the E_x field component in the $k_x d_i$ vs $k_y d_i$ plane at time $\Omega_{ci}t = 0.27$ (panel a) and $\Omega_{ci}t = 2.72$ (panel b). The spectra are calculated on the Refined Grid of the MLMD simulation with $RF = 8$.

that threshold, at $k_{sup,CG} \leq k < k_{sup,RG}$. This dataset will be used for further analysis in the next Sections.

Before proceeding to that, however, it is necessary to comment on the representation of spectra as cuts at an angle $\theta = 45°$ of the 2D spectra in the $k_x d_i$ vs. $k_y d_i$ plane. Undeniably, comparisons between spectra calculated in different cases (e.g., Figure 5 and 6) are done more easily if lines, rather than 2D plots, are compared. However, the choice of cuts at an angle $\theta = 45°$ in the $k_x d_i$ vs $k_y d_i$ plane may seem unusual for a current aligned instability like the LHDI. Figure 7 helps justifying this choice. The power spectra of E_x in the $k_x d_i$ vs $k_y d_i$ plane is represented at time $\Omega_{ci}t = 0.27$ (panel a) and $\Omega_{ci}t = 2.72$ (panel b). Data from the RG of the MLMD simulation with $RF = 8$ are shown. In panel a, $\Omega_{ci}t = 0.27$, one may notice that, as expected, power is stored preferentially in the wavenumber in the current aligned direction, x. Already in panel b, $\Omega_{ci}t = 2.72$ (the same time as Figure 6), the spectra has evolved in the direction of higher isotropy, thus better justifying our isotropic 1D representation.

B. Analysis of the mixed grid spectra

The mixed grid spectra of Figure 6 show a steepening in the slope of the δB_z power spectra, for all the three MLMD simulations, at $k_\perp d_i \sim 30$ (blue vertical line), which falls in the RG range of the mixed spectra. The fact that the steepening in the δB_z power spectra is observed at the same wavenumber for all the three simulations shows that it is a physical

process, rather than a numerical artefact. One can convince oneself of that by observing how the wavenumber marking the beginning of the E_x plateau (a resolution dependent artefact) shifts with the RF in Figure 6. This is not the case with the $k_\perp d_i$ slope change(a physical slope change).

The electric field power spectra, instead, do not experience any break at $k_\perp d_i = 30$.

The values of the slopes of the δB_z and E_x power spectra are calculated for the pre-break wavenumber range, at $1 < k_\perp d_i < 30$, for the three mixed grid datasets. Different times, $\Omega_{ci}t = 2.72$, $\Omega_{ci}t = 5.44$, $\Omega_{ci} = 8.16$, $\Omega_{ci}t = 10.88$ and $\Omega_{ci}t = 13.6$, are examined. MATLAB's *polyfit* function for least square polynomial fit is used with the data in log-log representation and with maximum degree of the polynomials $n = 1$ to find the slope of the spectra. The goodness of the fit is evaluated through the coefficient of determination R^2, which is calculated as

$$R^2 = 1 - \frac{SS_{res}}{SS_{tot}}. \tag{2}$$

SS_{res} is the sum of the squared residuals from the regression and SS_{tot} is the sum of the squared differences from the mean of the dependent variable. $R^2 = 1$ is a "perfect" fit. The values of the slopes and of the R^2 are listed in Table III and Table IV for the δB_z and the E_x field. One can notice a stark difference between the δB_z R^2 and the E_x R^2 values. While the R^2 in Table III are very good (if not excellent, especially at higher times) poorer performances are registered in Table IV. This may be partially due to the lower value (hence, lower variance) of the E_x spectra in presence of roughly comparable levels of oscillations around the fits of the δB_z and E_x fields.

At a given time, the three MLMD systems show remarkable good agreement. This can be noticed also in Figure 6, Figure 8 and Figure 9. The last two are analogues to Figure 6, but depict subsequent times, $\Omega_{ci}t = 5.44$ and $\Omega_{ci}t = 10.88$. $k_\perp d_i = 30$ is indicated as a blue vertical line in Figure 8 and 9 also. In all panels of all the three Figures, the E_x (δB_z) slopes calculated for $RF = 4$ (blue line), $RF = 6$ (red) and $RF = 8$ (green) are depicted together below (above) the spectra and in correspondence of the wave numbers used for the slope calculations. Notice that the three slopes are almost not distinguishable. The slope differences, at a fixed time, in Table III and Table IV can be explained because, in the different systems, a different number of data points is used for the slope calculations: $86 + 23$, $86 + 31$ and $86 + 47$ data points for $RF8$, $RF6$ and $RF4$ respectively. Of those, 86

	$RF4$		$RF6$		$RF8$	
	slope	R^2	slope	R^2	slope	R^2
$\Omega_{ci}t = 2.72$	-1.1021	0.6253	-0.8348	0.5206	-0.8458	0.5442
$\Omega_{ci}t = 5.44$	-1.3065	0.7364	-1.1196	0.6424	-1.1578	0.6457
$\Omega_{ci}t = 8.16$	-1.8201	0.8805	-1.7499	0.6901	-1.8731	0.8311
$\Omega_{ci}t = 10.88$	-2.3694	0.9239	-2.4230	0.9057	-2.1936	0.8586
$\Omega_{ci}t = 13.60$	-2.4764	0.9214	-2.4814	0.9039	-2.7002	0.8973

TABLE III. Slope and coefficient of determination R^2 of the δB_z power spectra calculated at $1 < k_\perp d_i < 30$ from the mixed coarse grid/ refined grid datasets for the MLMD simulations with $RF = 4$, $RF = 6$ and $RF = 8$ at times $\Omega_{ci}t = 2.72$, $\Omega_{ci}t = 5.44$, $\Omega_{ci} = 8.16$, $\Omega_{ci}t = 10.88$ and $\Omega_{ci}t = 13.6$.

	$RF4$		$RF6$		$RF8$	
	slope	R^2	slope	R^2	slope	R^2
$\Omega_{ci}t = 2.72$	-0.85427	0.4720	-0.86188	0.4791	-0.80658	0.4768
$\Omega_{ci}t = 5.44$	-0.51463	0.2244	0.60658	0.3504	-0.60783	0.3474
$\Omega_{ci}t = 8.16$	-0.62035	0.3585	-0.5516	0.4010	-0.69801	0.3418
$\Omega_{ci}t = 10.88$	-0.828	0.5272	-0.90982	0.5823	-0.95695	0.5158
$\Omega_{ci}t = 13.60$	-1.2114	0.6924	-1.3051	0.6150	-1.3467	0.7258

TABLE IV. Slope and coefficient of determination R^2 of the E_x power spectra calculated at $1 < k_\perp d_i < 30$ form the mixed coarse grid/ refined grid datasets for the MLMD simulations with $RF = 4$, $RF = 6$ and $RF = 8$ at times $\Omega_{ci}t = 2.72$, $\Omega_{ci}t = 5.44$, $\Omega_{ci} = 8.16$, $\Omega_{ci}t = 10.88$ and $\Omega_{ci}t = 13.6$.

are contributed from the coarse grid, the others from the refined grids.

One can notice that the slope of the spectra of δB_z increases with time, slightly between $\Omega_{ci}t = 2.72$ and $\Omega_{ci}t = 5.44$ and then more robustly from $\Omega_{ci}t = 5.44$ onwards. The slope of E_x decreases in absolute value between $\Omega_{ci}t = 2.72$ and $\Omega_{ci}t = 5.44$ and then increases. From $\Omega_{ci}t = 8.16$ onwards, the δB_z power spectra drop with $k_\perp$ at least twice faster than the E_x spectra. An explanation for this will be provided at the end of the Section. The

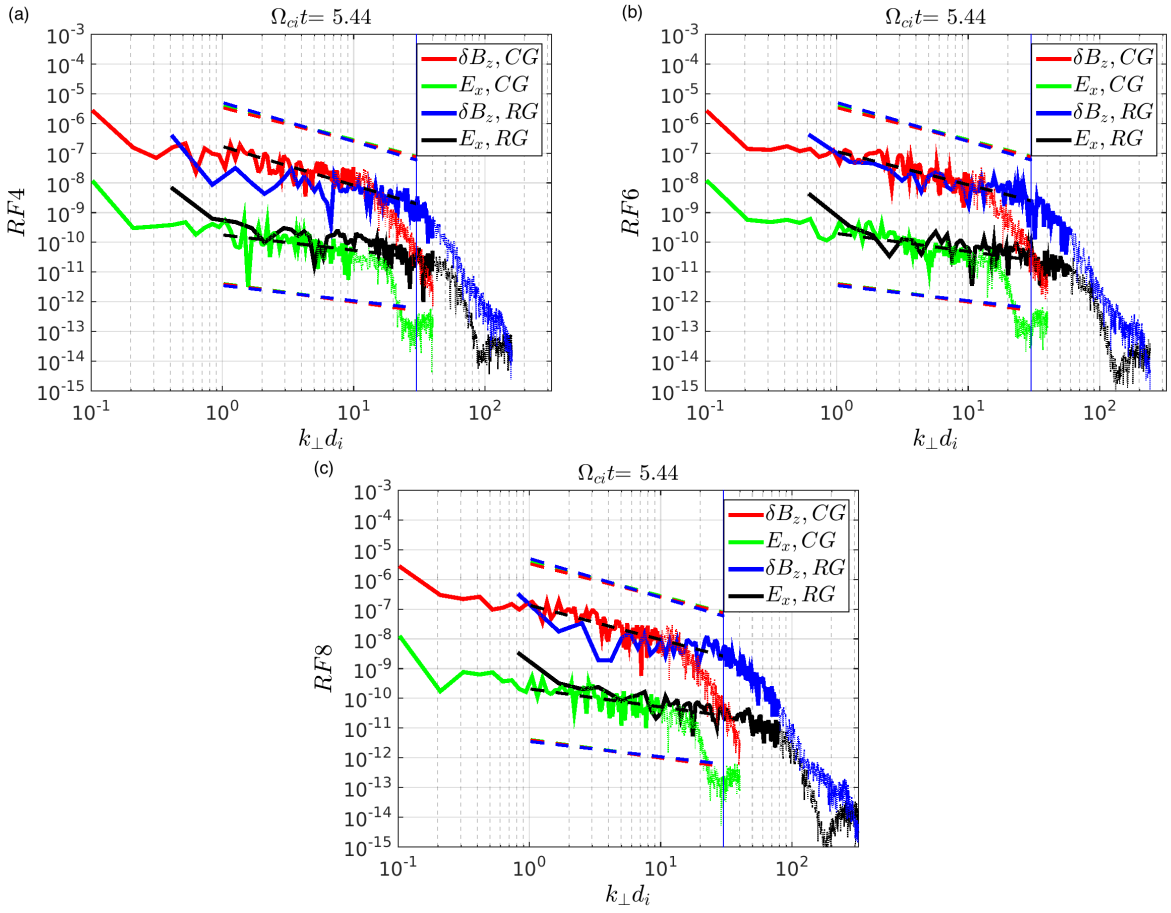

FIG. 8. Numerical power spectra of the fluctuations of the B_z (δB_z) and of the E_x field components as a function of $k_\perp$ at time $\Omega_{ci}t = 5.44$ for the MLMD simulations with $RF = 4$ (panel a), $RF = 6$ (panel b) and $RF = 8$ (panel c). The caption of Figure 6 is referred for further information.

slope increase with time is attributed to the development of slower electromagnetic branches, LHDI and kink. The break in the δB_z slope at wavenumber $k_\perp d_i = 30$ appears at the earliest times, together with the development of the fastest LHDI branches (it is already visible at $\Omega_{ci}t = 0.27$, not shown here). It becomes less visible at later times, as one can appreciate in Figure 8, time $\Omega_{ci}t = 5.44$. At time $\Omega_{ci}t = 10.88$, Figure 9, the break in the power spectra of δB_z has effectively disappeared.

An explanation for this behavior can be found recalling Norgren *et al.*[1].

There, LHDI fluctuations with $\omega/\Omega_{LH} \sim 1$ and $k_\perp r_e \sim 1$, as expected from the fast LHDI branch, are identified in Cluster data. The electrostatic potential $\Phi_{\delta E_\perp}$ associated with the

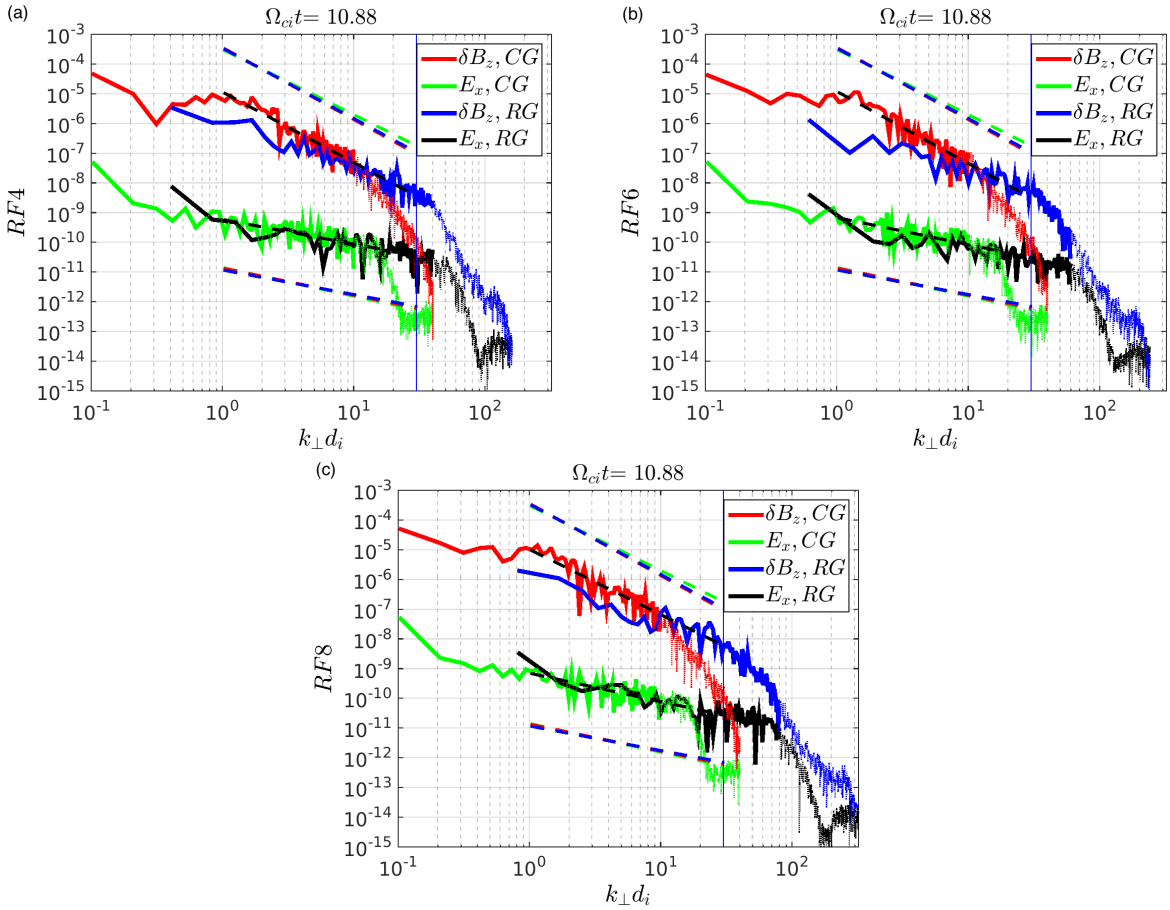

FIG. 9. Numerical power spectra of the fluctuations of the B_z (δB_z) and of the E_x field components as a function of $k_\perp$ at time $\Omega_{ci}t = 10.88$ for the MLMD simulations with $RF = 4$ (panel a), $RF = 6$ (panel b) and $RF = 8$ (panel c). The caption of Figure 6 is referred for further information.

waves is defined as:

$$\Phi_{\delta E_\perp} = \int \delta \mathbf{E}_\perp dt \cdot \mathbf{v}_{ph}, \tag{3}$$

where $\mathbf{v}_{ph}$ is the wave phase velocity. A potential associated to parallel magnetic field variations, $\Phi_{\delta B_\parallel}$, is defined based on assumptions associated to the nature of LHDI waves. First, perpendicular propagation, $k_\perp >> k_\parallel$, is assumed; hence,

$$\nabla \times \delta \mathbf{B} \sim k_\perp \delta B_\parallel, \tag{4}$$

where, as already in the simulations, $\delta \mathbf{B}$ labels the variations of the total magnetic field with respect to an "equilibrium" configuration where the LHDI has not developed. The corresponding variation in the perpendicular current is assumed to be carried by the electrons through $\mathbf{E} \times \mathbf{B}$ drift in the perturbed fields. In Norgren *et al.*[1], where an LHDI wave packet

with $k_\perp \sim 1/r_e$ is analysed (hence, $\mathbf{B}_\parallel \sim B_0$), the perpendicular current variation has the form

$$\delta J_\perp \sim e\rho_e \delta E_\perp / B_0, \tag{5}$$

where ρ_e is the electron density and e the electron charge. In the regions where the longer wavelength modes can be expected, i.e. where the "equilibrium" magnetic field is closer to zero, a dependence of the form:

$$\delta J_\perp \sim e\rho_e \delta E_\perp / \delta B_\parallel \tag{6}$$

instead holds. The linear relation between the perturbed perpendicular current and the perpendicular electric field (central to the investigations described in the rest of the Section) is preserved. Combining Eq. 4 and 5, the potential associated to $\delta B_\parallel$ perturbations can be written as:

$$\Phi_{\delta B_\parallel} = \frac{B_0}{\rho_e e \mu_0} \delta B_\parallel, \tag{7}$$

where μ_0 the permeability of free space. If a wavenumber $\mathbf{k}$ and a phase velocity $\mathbf{v}_{ph}$ can be found such that

$$\Phi_{\delta B_\parallel} \sim \Phi_{\delta E_\perp}, \tag{8}$$

those are taken as the wavenumber and the phase velocity of a wave package where a) propagation is mostly perpendicular (Eq. 4), b) a linear relation exists between the perturbations in the perpendicular electron current and the perpendicular electric field (Eq. 6) and c) most of the parallel magnetic field perturbations are due to electric field variations (Eq. 8). These conditions apply to both the fast and the slow LHDI branches, even if, as it will be explored in the next Section, the mechanism of oscillation coupling through the perpendicular current varies for the shorter and longer wavelengths. These considerations on coupling of electric and magnetic field fluctuations, with the perpendicular current as the mediator, can be exported to the MLMD simulations previously discussed. In the simulations, $\delta B_\parallel = \delta B_z$, the perpendicular plane is the simulation plane xy and B_0 is the Harris field value. One can then write the following relation between the electric and magnetic field spectra:

$$\tilde{E}_x = \frac{B_0}{\rho_e e \mu_0} k_\perp \tilde{\delta B}_z, \tag{9}$$

where the tilde indicates the spectra, rather than the power spectra as used up to now. Since no electric field is present at the beginning of the simulation, $\delta \mathbf{E}_\perp = \mathbf{E}_\perp$.

Figure 10 to Figure 12 intend to verify Equation 9 at different times, $\Omega_{ci} t = 0.27$ (Figure 10),

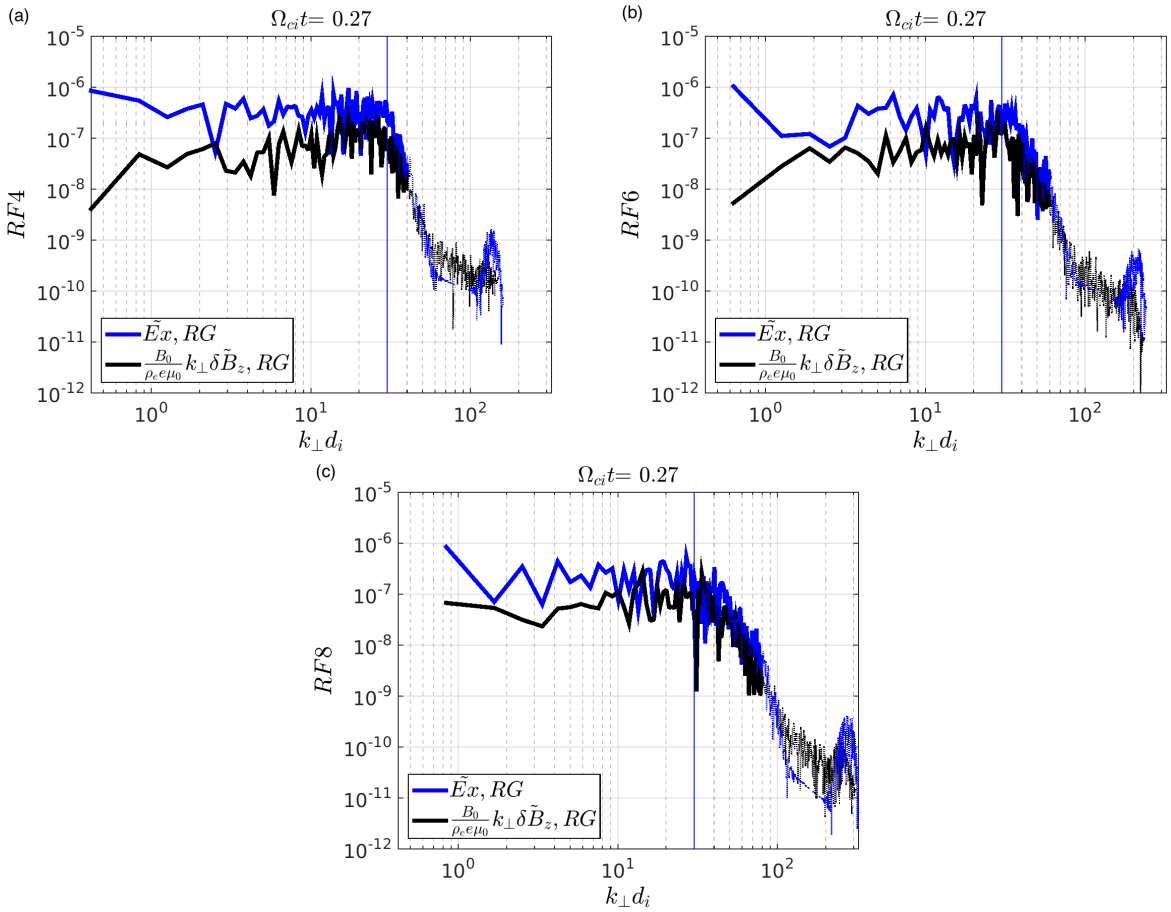

FIG. 10. Numerical spectra of E_x (blue line) and of δB_z multiplied by $\left(\frac{B_0}{\rho_e e\mu_0} k_\perp\right)$ as a function of $k_\perp$, oriented at $\theta = 45°$ in the k_x vs. k_y plane, at time $\Omega_{ci}t = 0.27$ for the Refined Grids of the MLMD simulations with $RF = 4$ (panel a), $RF = 6$ (panel b) and $RF = 8$ (panel c). The blue vertical line is $k_\perp d_i = 30$. The dotted lines mark the wavenumber ranges, $k_\perp > k_{max}/4$, which are deemed unreliable for physical investigations.

$\Omega_{ci}t = 5.44$ (Figure 11) and $\Omega_{ci}t = 10.88$ (Figure 12). Refined Grid data only are used. The blue lines in the Figures are the spectra of E_x, the blue lines the spectra of the magnetic field fluctuations multiplied by $k_\perp$, $B_0 = 0.0068$ and $\rho_e = 1$. Both the B_0 and the ρ_e values used are the respective peak values from in the Harris equilibrium configuration used as initial condition. $e = 1$ and $\mu_0 = 1$ in the normalisation used by the code.

In Figure 10, $\Omega_{ci}t = 0.27$, the $\frac{B_0}{\rho_e e\mu_0} k_\perp \delta\tilde{B}_z$ (black) and the $\tilde{E}_x$ (blue) lines are well superimposed in the $k_\perp d_i > 30$ interval for all the RF cases. The black lines are instead depressed with respect to the blues lines at lower wavenumbers. Increasingly better superposition, proceeding from the high towards the low wavenumber, is achieved at time $\Omega_{ci}t = 5.44$ (Fig-

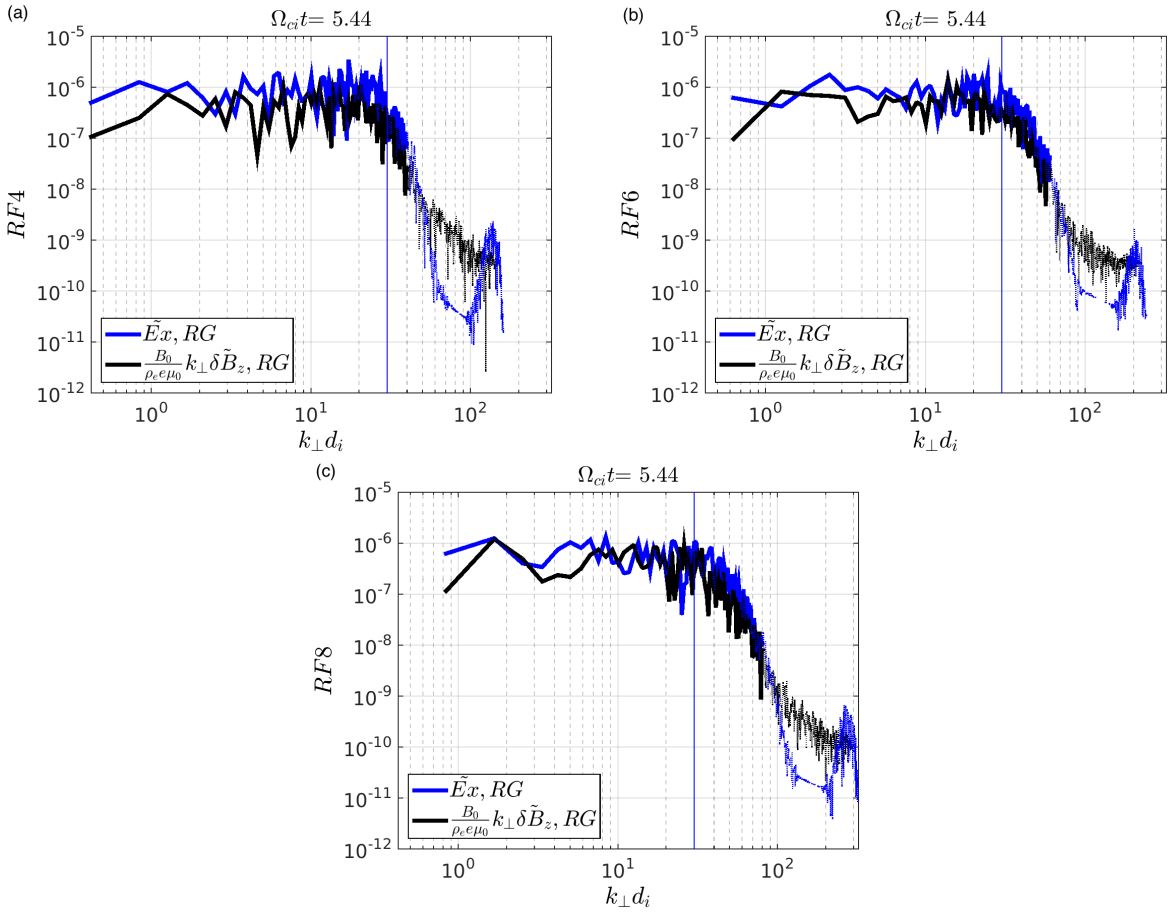

FIG. 11. Numerical spectra of E_x (blue line) and of δB_z multiplied by $\left(\frac{B_0}{\rho_e e \mu_0} k_\perp\right)$ as a function of $k_\perp$, oriented at $\theta = 45°$ in the k_x vs. k_y plane, at time $\Omega_{ci}t = 5.44$ for the Refined Grids of the MLMD simulations with $RF = 4$ (panel a), $RF = 6$ (panel b) and $RF = 8$ (panel c). The blue vertical line is $k_\perp d_i = 30$. The dotted lines mark the wavenumber ranges, $k_\perp > k_{max}/4$, which are deemed unreliable for physical investigations.

ure 11) and $\Omega_{ci}t = 10.88$ (Figure 12). The dotted part of the spectra, i.e. the one affected by numerical artefacts, should again not be taken in considerations for these analysis.

C. Spatial structure of current fluctuations

To understand why the black and blue lines in Figures 10 to 12 superimpose (or not) at different times, it is convenient to remind oneself of the origin of the coupling between electric and magnetic field fluctuations. In the derivation just recalled, it is mediated by perpendicular electron current due to electron $\mathbf{E} \times \mathbf{B}$ drift into the "modified" fields.

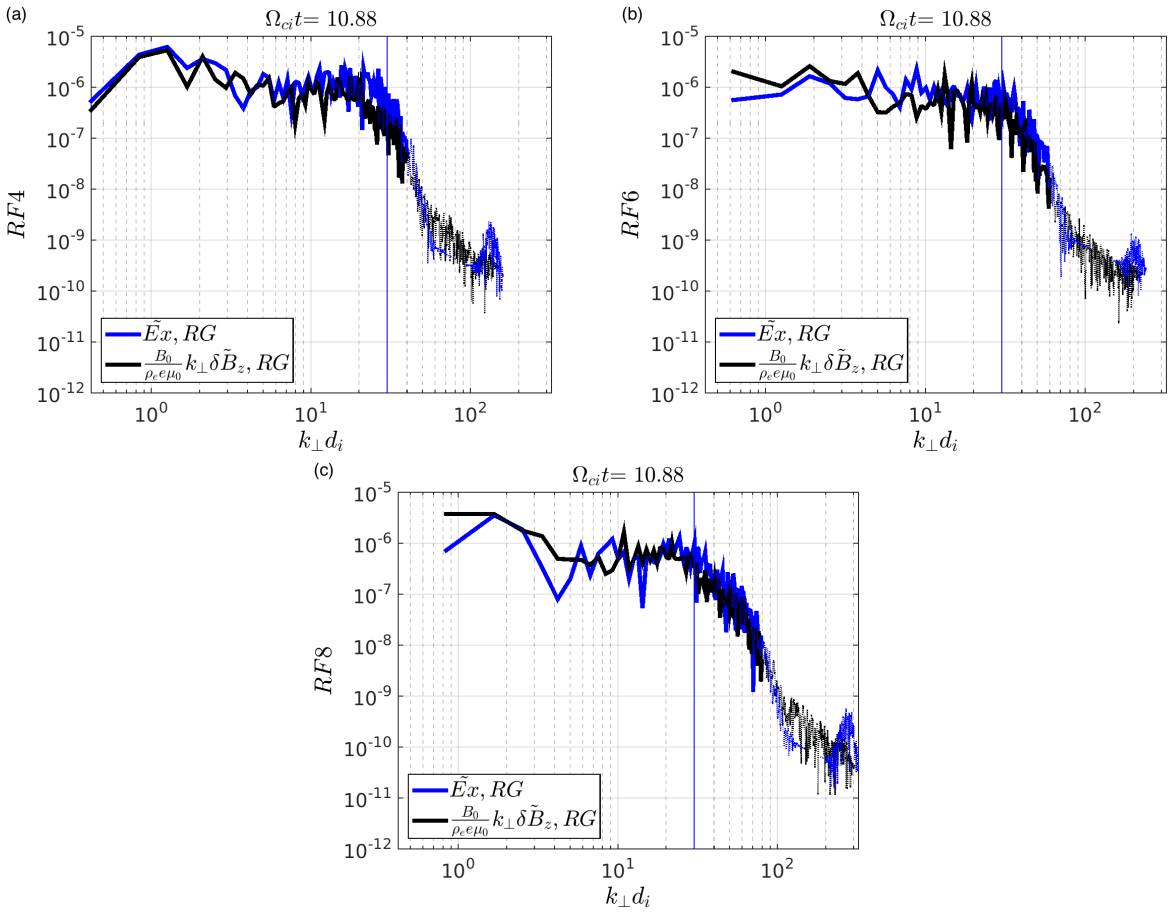

FIG. 12. Numerical spectra of E_x (blue line) and of δB_z multiplied by $\left(\frac{B_0}{\rho_e e\mu_0} k_\perp\right)$ as a function of $k_\perp$, oriented at $\theta = 45°$ in the k_x vs. k_y plane, at time $\Omega_{ci}t = 10.88$ for the Refined Grids of the MLMD simulations with $RF = 4$ (panel a), $RF = 6$ (panel b) and $RF = 8$ (panel c). The blue vertical line is $k_\perp d_i = 30$. The dotted lines mark the wavenumber ranges, $k_\perp > k_{max}/4$, which are deemed unreliable for physical investigations.

It can be verified that, already at time $\Omega_{ci}t = 0.27$, the electron current in both perpendicular directions is indeed given by $\mathbf{E}\times\mathbf{B}$ drift (the electron contribution to the equilibrium current is quite weak with respect to the ions with the current set of Harris equilibrium parameters). E_x, $J_{el,y}$ and B_z are then related as in:

$$\mathbf{J}_{el} = e\rho_{el}\frac{\mathbf{E}\times\mathbf{B}}{B^2}. \tag{10}$$

Figure 13 shows a zoom of E_x (panel a), contrasted with the corresponding electron current component, $J_{y,el}$ (panel b), at time $\Omega_{ci}t = 0.27$. The refined grid of the simulation with $RF = 8$ is shown. One immediately notices the correspondence between the traces at the

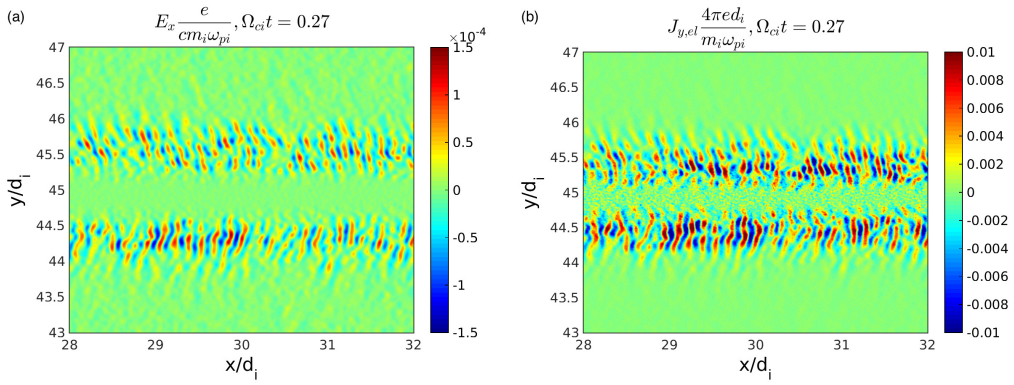

FIG. 13. Signature of the development of the high-wavenumber, mostly electrostatic LHDI branch, mode "A", in E_x (panel a) and $J_{y,el}$ (panel b) at time $\Omega_{ci}t = 0.27$ and $28 < x/d_i < 32$, $43 < y/d_i < 47$ in the Refined Grid of the MLMD simulation with $RF = 8$.

edges of the current sheet in the two plots. The electric field traces are the characteristic signatures of the fast LHDI branch, indicated as mode "A" in the introduction. Electrons respond immediately to that and corresponding traces in the electron current ensue. These fluctuations in the in-plane current couple the high wavenumber fluctuations in E_x and δB_z in Figure 10. No larger scale fluctutations are observed in the current plots, thus explaining the lack of coupling in the lower wavenumber range.

Better coupling at larger wavelength in Figure 11, at time $\Omega_{ci}t = 5.44$, corresponds to electron current fluctuations located at the centre of the current sheet, $y/d_i \sim 45$, in Figure 14, panel a. Figure 14 shows the development at the center of the current sheet of the mostly electromagnetic LHDI branch characterised in Daughton[36], mode "B" in the introduction. The current fluctuation at the center of the current sheet in panel (a) are visibly larger than the fluctuations at the edges of the current sheet already seen in Figure 13 and still visible here. A first analysis of E_x at time $\Omega_{ci}t = 5.44$ reveals fluctuations at the edges of the current sheet, but no evident correspondence for the larger current structures. This is because the E_x fluctuations resulting in $J_{y,el}$ structures at $y/d_i \sim 45$ are weaker than the fast LHDI signatures, but are also located in an area where $B_z \to 0$ and experiences the kink visible in Figure 14, panel b. The kinking of the neutral line explains the pattern of the $J_{y,el}$ structures at $y/d_i \sim 45$ and is in turn due to the development of the slower, electromagnetic branch of the LHDI, as it can be verified by comparing Figure 14, panel (b) and (c). Panel

(c) depicts the electromagnetic (EM) component of E_y, calculated as in Lapenta *et al.*[83]:

$$\mathbf{E}_{ES} = \nabla \left[\nabla^{-2} \left(\nabla \cdot \mathbf{E}\right)\right]; \mathbf{E}_{EM} = \mathbf{E} - \mathbf{E}_{ES}, \tag{11}$$

where ES is the electrostatic component. The length of the $E_{y,EM}$/ $J_{el,y}$ traces is of the order of $\ell/d_i \sim 0.15 - 0.3$, which corresponds to $k_\perp d_i \sim 20 - 40$, in good agreement both with the expected prevalent wavelength of the electromagnetic LHDI mode, $k_\perp \sim 1/\sqrt{r_i r_e} \sim 20 d_i$, and with the position of the δB_z spectral break at low simulated time, $k_\perp d_i \sim 30$. Figure 14 thus accounts for the closer coupling between black and blue lines at intermediate wavenumbers in Figure 11. Conversely, it explains the poorer coupling at earlier times and, as a consequence, the presence of a break in the power spectra of δB_z at times when the EM LHDI component has not fully developed yet (see Section III B). Figure 15 highlights the ion response to electromagnetic electric field fluctuations at a later time, $\Omega_{ci} t = 10.88$. Panel (a) and (b) are $E_{x,EM}$ and the drift velocity of the background ion, $V_{y,ion,BG}$. At this time, large kink fluctuations have formed in both $E_{x,EM}$ and $E_{y,EM}$. The electromagnetic LHDI fluctuations are still visible in correspondence of the kinked neutral layer as dents embedded in the larger structures. The electron current (not shown here) reacts very similarly to Figure 14, showing a response to both the electromagnetic and electrostatic LHDI fields. It does not react to the electromagnetic fluctuation generated by the kinking instability. Instead, $V_{y,ion,BG} = (\mathbf{E}_{EM} \times \mathbf{B})/|\mathbf{B}|$. The fact that only the background ions respond to the electromagnetic oscillations hints to a ion-ion drift instability (IIDI) rather than to an (electron-ion) drift kink instability[49,50]. The $k_x d_i$ vs $k_y d_i$ spectrum of the total ion current in the y direction, $J_{y,ion}$, is examined. The CG (the refined grid k resolution is too low for wavelengths this long) 2D spectrum of $J_{y,ion}$ at time $\Omega_{ci} t = 10.88$ shows increased power in a wavenumber range ending with $k_x d_i \sim 2$. The expected wavenumber for the IIDI is $k_x L_H \sim 1$, which corresponds to $k_x d_i \sim 1.9$ here, where $L_H/d_i = 0.53$.

Figure 10 and 13 confirm the observations of Norgren *et al.*[1] regarding magnetic and electric field fluctuation coupling through the perpendicular electron current in correspondence of the fast, high wavenumber branch of the LHDI instability. Figure 11, 12, 14 and 15 hint at the possibility of extending the coupling to the wavenumbers corresponding to the slower LHDI branch. The mediator for the coupling is in both cases the in plane electron current. In the next Section, this possibility of $E_\perp/\delta B_z$ coupling at lower wavenumber is

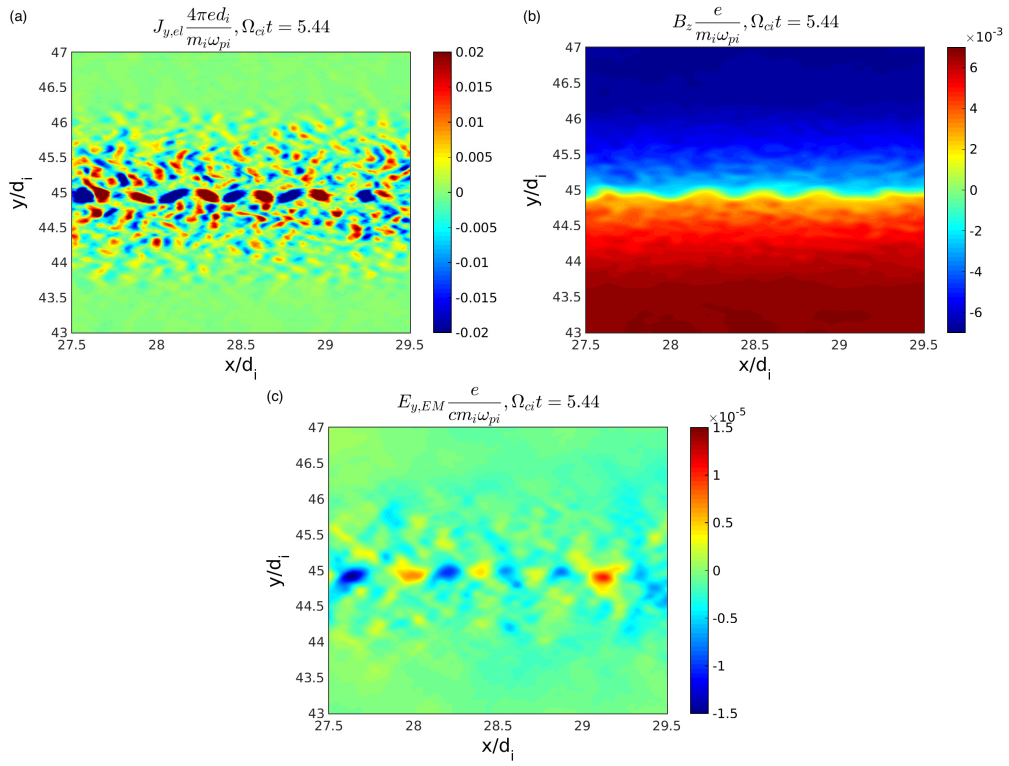

FIG. 14. Signature of the development of the low-wavenumber, mostly electromagnetic LHDI branch, mode "B", in $J_{y,el}$ (panel a), B_z (panel b) and $E_{EM,y}$ (panel c) at time $\Omega_{ci}t = 5.44$ and $27.5 < x/d_i < 29.5$, $43 < y/d_i < 47$ in the Refined Grid of the MLMD simulation with $RF = 8$. The traces in $E_{EM,y}$ correspond to $k_\perp d_i \sim 20 - 40$, with $k_\perp \sim 1/\sqrt{r_i r_e} \sim 20 d_i$ the wavenumber expected from Daughton [36] for the mostly electromagnetic LHDI branch developing at the center of the current sheet.

verified though Cluster observations.

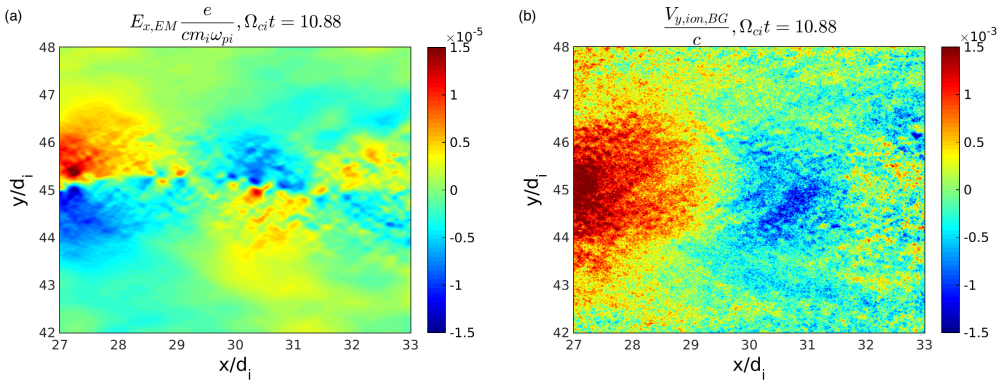

FIG. 15. Signature of the development of an electromagnetic kinking mode, mode "C", in $E_{x,EM}$ (panel a) and in the drift velocity of the background ions, $V_{y,ion,BG}$, (panel b) at time $\Omega_{ci}t = 10.88$ and $27.5 < x/d_i < 29.5$, $43 < y/d_i < 47$ in the RG of the MLMD simulation with $RF = 8$. The ion current spectrum shows a peak at $k_x d_i \leq 2$. The expected wavenumber for the IIDI from Karimabadi *et al.*[49] is $k_x L_H \sim 1$, which corresponds to $k_x d_i \sim 1.9$ here, where $L_H/d_i = 0.53$.

IV. CLUSTER SPACECRAFT OBSERVATIONS

In Norgren *et al.*[1], coupling between electric and magnetic field oscillations is demonstrated at the small wavelengths associated with the mostly electrostatic LHDI branch. In this Section, the same methodology illustrated in Norgren *et al.*[1] is used on different data intervals. We demonstrate here coupling between electric and magnetic field oscillations at both the high wavenumbers associated with the mostly electrostatic LHDI branch (as already done in Norgren *et al.*[1]) *and* at the lower wavenumbers associated with the mostly electromagnetic LHDI branch. The latter part is shown here for the first time and confirms the simulation results: when both LHDI branches are present, as in Figure 12, the coupling between magnetic and electric field oscillations already demonstrated in Cluster data at high wavenumbers is present over the entire LHDI unstable spectrum.

Data from September 2, 2007, are presented, when Cluster 3 was located in the magnetotail at $[-10 \; -3 \;\; 3]$ Earth radii in geocentric solar magnetospheric (GSM) coordinates and encountered the plasma sheet boundary layer and an earthward going ion jet (Figure 16, panel a, b and c). Here and in all the following occurrences, three values enclosed in square brackets indicate the three spatial components in the GSM coordinate system. At the time investigated here, both the magnetic field (Figure 16, panel a) and the electric

field (Figure 16, panel c) show wave activity around Ω_{LH}. The waves observed during the interval marked with a thick yellow line in Figures 16, panel a, b and c, are investigated in detail. During this time interval, $\rho = 0.45$ cm^{-3}, $B_0 = 32$ nT, $T_e = 1.8$ keV and $T_i = 5.8$ keV. The associated physical lengths are $d_i = 142$ km, $r_i = 242$ km, and $r_e = 3.4$ km. As already in Norgren *et al.*[1], which is referenced for further details on the methodology, the phase velocities perpendicular to **B** and subsequent length scales are obtained by finding the best match between $\Phi_{\delta E_\perp}$ (Equation 3) and $\Phi_{\delta B_{||}}$ (Equation 7). Recalling the derivation in Section III B, one can notice that the best match is subject to the choice of a particular perpendicular wave vector: at the end of the matching procedure, we will obtain the wavenumber at which electric and magnetic field oscillations match best for oscillations at a particular frequency. To investigate different time and length scales, **E** and **B** are highpass-filtered at two different frequencies.

Figure 16, panel d, shows the potentials $\Phi_{\delta E_\perp}$ (red) and $\Phi_{\delta B_\parallel}$ (orange) obtained for $\omega > 0.1\Omega_{LH}$. The potentials show excellent agreement at the phase speed $\mathbf{v}_{ph} = 430 \times [0.61\ -0.41\ -0.68]_{GSM}$ km/s. The wavelength of best match is about 150 km (see axis on top of panel), corresponding to $5.5\sqrt{r_e r_i}$, which is in good agreement with the expected length scales of the more slowly growing modes of the LHDI. The ratio between the maximum electric and magnetic fields is $\delta E_{max}/\delta B_{max} = 0.06c$: the mode is mostly electromagnetic.

In short: we have filtered the signal at frequencies corresponding to those of the slow, electromagnetic LHDI branch. We have found excellent coupling between electric and magnetic field oscillations at a wavenumber which corresponds to the expected wavenumber of the electromagnetic LHDI branch. The $\delta E_{max}/\delta B_{max}$ ratio shows that the mode is electromagnetic in nature. Hence, we have verified electric and magnetic field oscillation coupling of the electromagnetic LHDI mode. Now, we search for evidence of the coupling for the electrostatic branch as well. To do that, the filtering is done at the appropriate, higher frequency of $\omega > 0.5\Omega_{LH}$. Figure 16, panel e, shows the electrostatic potentials obtained after the filtering. It shows excellent agreement for most part of the time interval at a slightly lower phase speed $\mathbf{v}_{ph} = 320 \times [0.63\ -0.48\ -0.61]_{GSM}$ km/s. The wavelength is about 24 km, corresponding to $7r_e$. This wavelength is in good agreement with the expected length scales for the more rapidly growing modes of the LHDI. For these shorter wavelengths the magnetic field is relatively weaker, $\delta E_{max}/\delta B_{max} = 0.29c$, than for the long wavelengths. In this case, with the filtering done at the higher frequencies associated to the electrostatic

LHDI branch, the wavelength of best match is found to be indeed the one expected for the fast LHDI branch. Also, the $\delta E_{max}/\delta B_{max}$ ratio confirms that the oscillations are electrostatic in nature: we have verified that, in the Cluster data interval of interest, both the electrostatic and the electromagnetic LHDI oscillations are present and that, in both cases, the coupling between electric and magnetic field oscillation, at the respective wavenumbers, is remarkable.

Figure 17 further demonstrates oscillation coupling over a large wavenumber range .

Panel a shows the power spectra of $\Phi_{\mathbf{B}_\parallel}$ and $\Phi_{\mathbf{E}_\perp}$, as a function of the normalised perpendicular wavenumber $k_\perp d_i$, obtained during the time interval in between the sharpest gradients in the magnetic field: $15:47:05-15:48:10$. To calculate the spectra of $\Phi_{\mathrm{B}_\parallel}$, local values for the density and ambient magnetic field are used. To calculate the spectra of $\Phi_{\mathrm{E}_\perp}$, the electric field is integrated in Fourier space: $\mathbf{E}\cdot\mathbf{v_{ph}}/\omega$, using a single phase velocity $\mathbf{v}_{\mathrm{ph}} = 430\times[0.61\ -0.41\ -0.68]_{GSM}$ km/s (as in Figure 16, fourth d). Variations in $\mathbf{v}_{\mathrm{ph}}$ in time, or between different length and time scales (as seen between panel d and e of Figure 16) may introduce some errors in the spectra of $\Phi_{\mathrm{E}_\perp}$ which are not taken into account here. The spectra of $\Phi_{\mathrm{B}_\parallel}$ and $\Phi_{\mathbf{E}_\perp}$ show good correlation along the major range of wavenumbers depicted, from $kr_i\sim 1$ (green line) through $k\sqrt{r_e r_i}\sim 1$ (purple line) and beyond $kr_e\sim 1$ (blue line), indicating that the phase velocity used can at least be considered representative for the major part of the wavenumber interval.

From the present set of observational data, it is not possible to determine if and at what high wavenumber the coupling between $\Phi_{\mathrm{E}_\perp}$ and $\Phi_{\mathrm{B}_\parallel}$ breaks down. The higher end of the spectra is limited due to the sampling frequency, $f_s = 450$ Hz, of $\mathbf{E}$ and $\mathbf{B}$ and the noise level of the magnetic field instrument.

The good correlation between the spectra of $\Phi_{\mathrm{E}_\perp}$ and $\Phi_{\mathrm{B}_\parallel}$ over this wavenumber range is expected from the investigation in Section III B in presence of both LHDI branches.

Figure 17, panel b, shows the power spectra of the parallel magnetic field (orange line, left axis) and of the perpendicular electric field (red line, right axis) below and above $k_\perp r_e\sim 1$, when the slopes change. No slope change is observed at $k_\perp\sqrt{r_i r_e}\sim 1$, confirming that both fast and slow LHDI branches are present. Consistently, the slope values pre-breaks, -0.63 and -2.63 for the electric and magnetic field respectively, are compatible (albeit loosely) with times, in Table III and IV, when the slow LHDI branch has already developed.

V. CONCLUSIONS

Fluctuations in the electric and magnetic fields in the terrestrial magnetotail due to the Lower Hybrid Drift Instability are studied with realistic mass ratio fully kinetic simulations performed with the semi-implicit adaptive Multi-Level Multi-Domain method. The MLMD method (recapped in Section II) is used as a way to reduce the cost of PIC simulations without compromising on resolution, domain size or value of the physical parameters. Also, it is used as a cheap tool for convergence studies. It is particularly needed in cases, such as turbulence studies, where spectra are a key investigation method: the PIC approach in fact introduces numerical artefact in the high wavenumber part of the spectrum.
In Section III, realistic mass ratio MLMD simulations of LHDI instability are shown. Different jumps in the spatial resolution between the coarse and refined MLMD grids (Refinement Factor, RF) are used. Simulations with different RFs are compared for validation purposes: physical processes are independent of the grid resolution. In Section III A, a critical result for the applicability of the MLMD method to turbulence simulations is shown. RG spectra are compared with those of a single grid simulation with comparable parameters. It is shown that the MLMD CG drives the RG spectra in the wavenumber range of overlap to values similar to CG values. Single grid simulations are instead not able to develop those low k modes independently.

In Section III B a"mixed grid spectrum" is used for the computation of the slope of the power spectra of E_x and δB_z. The mixed grid spectra depicted in Figure 6, 8 and 9 in Section III B offer the possibility of commenting more extensively on the use of the MLMD method for turbulence simulations. Three areas can be identified in Figure 6, 8 and 9: a $k_\perp$ region simulated only by the coarse grid (region 1), one simulated by both the coarse and the refined grid (region 2), one simulated only by the refined grid (region 3). The k interval affected by numerical artefacts is neglected in the present discussion. A "successful" simulation of turbulence with the MLMD method should be able to correctly simulate the energy transfer between a driver located in region 1 in k space and a sink located in region 3. Region 2, simulated both by the coarse and the refined grid, is essential to achieve this result. The high wavenumber part of RG spectra in region 2 is not directly forced by the CG, but develops naturally as a result of RG evolution. Having the CG and RG spectra superimpose there (as it happens in Figure 6, 8 and 9) means that the boundary condition

forcing from the CG to the RG is sufficient to initiate the energy cascade in the RG, which is now simulating it independently and consistently with the CG solution. If CG and RG spectra superimpose at the end of region 2 (meaning, just before the "invalid" CG area), it is reasonable to expect that the energy cascade will continue without major method-induced problems in the region simulated only by the CG.

A break at $k_\perp d_i \sim 30$ in the slope of the power spectra of δB_z is observed in the mixed grid spectra at times when the slower electromagnetic branch of the LHDI has not developed yet. The relation between the fluctuations of the perpendicular electric field and those of the magnetic field observed by Norgren *et al.*[1] in LHDI waves in the terrestrial magnetotail is applied to the simulation data. It is concluded that the spectral break is related to the lack of coupling between electric field and magnetic field fluctuations, at early simulated times ($\Omega_{ci}t < 5.44$), in the intermediate and low wavenumber range. High, intermediate and low wavenumber ranges are defined as the ranges where the electrostatic LHDI, electromagnetic LHDI and kink instability are respectively dominant. Since Norgren *et al.*[1] identifies in the perpendicular current the coupling agent between electric and magnetic field fluctuations, the spatial structure of the y component of the current is studied in Section III C. It is indeed verified that coupling is achieved, at certain wavenumbers, when the in-plane current responds to the electric field fluctuations at that scale. Coupling in the high wavenumber (electrostatic LHDI) range is observed immediately because the electron current immediately responds to the short wavelength LHDI fluctuations. Intermediate range coupling is obtained when the electron current fluctuates at the scales dictated by the electromagnetic LHDI traces which are visible in the centre of the current sheet from approximately $\Omega_{ci}t > 5.44$ onwards. Cluster observations confirm the coupling of electric and magnetic field oscillations over the entire LHDI wavenumber range, in cases when both the electrostatic and the electromagnetic LHDI branches have developed.

Appendix A GRID RELATED EFFECTS ON POWER SPECTRA: FIELD SMOOTHING

It will be examined now how the spectral structures identified in Section III A in the "non reliable" wavenumber range, $k_\perp > k_{sup}$, are related to the use of field smoothing.

Field smoothing is used to curb the numerical noise in PIC simulations and to contrast the

development of numerical instabilities[84–86]. It removes energy from the higher frequencies and wave numbers through what can be described, at the simplest level, as an averaging routine: the value of a field at a grid point is obtained by averaging the pre-smoothing values of its nearest neighbors. The averaging routine is applied, in the code used in this study, to the variables (electric field at the previous time step, particle moments) used in the Right Hand Side of the equation solved for the time-updated value of the electric field, Eq. 26 in Innocenti *et al.*[33]. Since smoothing affects the higher wavenumber range and is related to the spatial resolution, it is a primary candidate to explain the origin of the numerical artefacts observed in the $k_\perp > k_{sup}$ part of the numerical spectra.

Different levels of smoothing may be used in a simulation, i.e. the smoothing routine may be applied a different number of times per cycle. In the simulations analyzed in the previous Sections, a smoothing level of $Sm = 5$ is used. Now, the spectra of single level simulations where different levels of smoothing are used will be compared. The single level simulations have parameters corresponding to the Coarse Grids of the MLMD simulation examined in Section III.

Figure A18 shows the numerical power spectra at different times of δB_z and of E_x as a function of the perpendicular wavenumber for a simulation with smoothing level $Sm = 5$. The times represented are $\Omega_{ci}t = 0.272$ (black line), $\Omega_{ci}t = 2.72$ (cyan), $\Omega_{ci}t = 5.44$ (red), $\Omega_{ci}t = 8.16$ (green), $\Omega_{ci}t = 10.88$ (blue) and $\Omega_{ci}t = 13.6$ (yellow). The black dash-dotted line represents the spectra at a very early time, $\Omega_{ci}t = 0.01$, before the development of the instabilities. It can therefore be used as a proxy for the noise level in the simulations. The increase in time of the power spectra of δB_z and E_x in the reliable wavenumber range, $k_\perp d_i < k_{sup} d_i = 10$ (see Table I), is due the development of the low-wavenumber LHDI branches and of ion ion kink modes[49,50] not suppressed by the realistic mass ratio. Figure A19 shows a simulation performed with the same initial conditions of Figure A18, but with a different level of smoothing, $Sm = 3$. The high wavenumber structure in the electric field spectra is qualitatively very similar to the one observed in Figure A18, but it is pushed to higher wavenumbers evidently by the use of a reduced level of smoothing. The location of the knee in E_x, red vertical line, shifts from $k_\perp\, d_i \sim 16$ with $Sm = 5$ to $k_\perp\, d_i \sim 19$ with $Sm = 3$. The location of the plateau, green vertical line, moves from $k_\perp\, d_i \sim 23$ with $Sm = 5$ to $k_\perp\, d_i \sim 29$ with $Sm = 3$. Also, as expected[84,86], the value of the plateau is higher when a reduced level of smoothing is used.

In the simulation depicted in Figure A20, no smoothing is used. The most immediate consequence is the increase in power of the electric field component of the spectra, Figure A20, bottom panel. Secondarily, the structures in E_x have disappeared and can therefore be rather confidently related to smoothing. However, even if the artefacts more directly related to the electric field signatures (red and green vertical lines in Figure A18 and Figure A19) have been levelled off, the change in slope in the spectra of δB_z in correspondence of the blue vertical line, $k_\perp d_i \sim 10$, has survived the absence of smoothing: it is evidently related to grid effects other than smoothing. The relation of this structure to the spatial resolution has been explored in Section III A.

The absence of smoothing has very negative impact on energy conservation. Cohen *et al.*[87] remarks on the importance of smoothing for energy conservation especially when the algorithm is semi-implicit. For this reason, smoothing is retained notwithstanding its correlation with the appearance of numerical artefacts in the E_x spectra.

ACKNOWLEDGMENTS

This work has received funding from the Onderzoekfonds KU Leuven (Research Fund KU Leuven). We acknowledge PRACE for awarding us access to SuperMUC, based in Germany at Leibniz Supercomputing Centre, contract N 2013091928, and NERSC, a DOE Office of Science User Facility supported by the Office of Science of the U.S. Department of Energy, Contract N. DE-AC02-05CH11231. M.E.I. is funded by an FWO (Fonds Wetenschappelijk Onderzoek) post-doctoral fellowship, grant number 12O5215N.

REFERENCES

[1]C. Norgren, A. Vaivads, Y. V. Khotyaintsev, and M. André, "Lower hybrid drift waves: Space observations," Physical review letters **109**, 055001 (2012).

[2]A. N. Kolmogorov, "A refinement of previous hypotheses concerning the local structure of turbulence in a viscous incompressible fluid at high reynolds number," Journal of Fluid Mechanics **13**, 82–85 (1962).

[3]J. Klimchuk, "On solving the coronal heating problem," Solar Physics **234**, 41–77 (2006).

[4]J. V. Hollweg, "Transition region, corona, and solar wind in coronal holes," Journal of Geophysical Research: Space Physics **91**, 4111–4125 (1986).

[5]S. R. Cranmer, A. A. Van Ballegooijen, and R. J. Edgar, "Self-consistent coronal heating and solar wind acceleration from anisotropic magnetohydrodynamic turbulence," The Astrophysical Journal Supplement Series **171**, 520 (2007).

[6]P. J. Coleman, Jr., "Turbulence, Viscosity, and Dissipation in the Solar-Wind Plasma," **153**, 371 (1968).

[7]R. Bruno and V. Carbone, "The solar wind as a turbulence laboratory," Living Reviews in Solar Physics **2**, 4 (2005).

[8]E. Yordanova, A. Vaivads, M. André, S. Buchert, and Z. Vörös, "Magnetosheath plasma turbulence and its spatiotemporal evolution as observed by the cluster spacecraft," Physical review letters **100**, 205003 (2008).

[9]O. Alexandrova, C. Lacombe, A. Mangeney, R. Grappin, and M. Maksimovic, "Solar wind turbulent spectrum at plasma kinetic scales," The Astrophysical Journal **760**, 121 (2012).

[10]S. Huang, F. Sahraoui, X. Deng, J. He, Z. Yuan, M. Zhou, Y. Pang, and H. Fu, "Kinetic turbulence in the terrestrial magnetosheath: Cluster observations," The Astrophysical Journal Letters **789**, L28 (2014).

[11]F. Sahraoui, S. Huang, G. Belmont, M. Goldstein, A. Rétino, P. Robert, and J. De Patoul, "Scaling of the electron dissipation range of solar wind turbulence," The Astrophysical Journal **777**, 15 (2013).

[12]F. Sahraoui, M. Goldstein, P. Robert, and Y. V. Khotyaintsev, "Evidence of a cascade and dissipation of solar-wind turbulence at the electron gyroscale," Physical review letters **102**, 231102 (2009).

[13]R. J. Leamon, W. H. Matthaeus, C. W. Smith, and H. K. Wong, "Contribution of cyclotron-resonant damping to kinetic dissipation of interplanetary turbulence," The Astrophysical Journal Letters **507**, L181 (1998).

[14]S. P. Gary and J. E. Borovsky, "Alfvén-cyclotron fluctuations: Linear vlasov theory," Journal of Geophysical Research: Space Physics (1978–2012) **109** (2004).

[15]D. Biskamp, *Magnetic reconnection in plasmas*, Vol. 3 (Cambridge University Press, 2005).

[16]A. Lazarian and E. T. Vishniac, "Reconnection in a weakly stochastic field," The Astrophysical Journal **517**, 700 (1999).

[17]D. Sundkvist, A. Retinò, A. Vaivads, and S. D. Bale, "Dissipation in turbulent plasma due to reconnection in thin current sheets," Physical review letters **99**, 025004 (2007).

[18]A. Retinò, D. Sundkvist, A. Vaivads, F. Mozer, M. André, and C. Owen, "In situ evidence of magnetic reconnection in turbulent plasma," Nature Physics **3**, 236–238 (2007).

[19]S. Servidio, F. Valentini, F. Califano, and P. Veltri, "Local kinetic effects in two-dimensional plasma turbulence," Physical review letters **108**, 045001 (2012).

[20]K. Osman, W. Matthaeus, J. Gosling, A. Greco, S. Servidio, B. Hnat, S. C. Chapman, and T. Phan, "Magnetic reconnection and intermittent turbulence in the solar wind," Physical Review Letters **112**, 215002 (2014).

[21]H. Che, J. Drake, and M. Swisdak, "A current filamentation mechanism for breaking magnetic field lines during reconnection," Nature **474**, 184–187 (2011).

[22]W. Daughton, V. Roytershteyn, H. Karimabadi, L. Yin, B. Albright, B. Bergen, and K. Bowers, "Role of electron physics in the development of turbulent magnetic reconnection in collisionless plasmas," Nature Physics **7**, 539–542 (2011).

[23]V. Olshevsky, A. Divin, E. Eriksson, S. Markidis, and G. Lapenta, "Energy Dissipation in Magnetic Null Points at Kinetic Scales," **807**, 155 (2015).

[24]V. Roytershteyn, W. Daughton, H. Karimabadi, and F. S. Mozer, "Influence of the lower-hybrid drift instability on magnetic reconnection in asymmetric configurations," Phys. Rev. Lett. **108**, 185001 (2012).

[25]T. Dannert and F. Jenko, "Gyrokinetic simulation of collisionless trapped-electron mode turbulence," Physics of Plasmas (1994-present) **12**, 072309 (2005).

[26]G. G. Howes, J. M. TenBarge, W. Dorland, E. Quataert, A. A. Schekochihin, R. Numata, and T. Tatsuno, "Gyrokinetic simulations of solar wind turbulence from ion to electron scales," Physical review letters **107**, 035004 (2011).

[27]D. Perrone, F. Valentini, S. Servidio, S. Dalena, and P. Veltri, "Vlasov simulations of multi-ion plasma turbulence in the solar wind," The Astrophysical Journal **762**, 99 (2013).

[28]L. Franci, A. Verdini, L. Matteini, S. Landi, and P. Hellinger, "Solar wind turbulence from mhd to sub-ion scales: High-resolution hybrid simulations," The Astrophysical Journal Letters **804**, L39 (2015).

[29]E. Camporeale and D. Burgess, "The dissipation of solar wind turbulent fluctuations at electron scales," The Astrophysical Journal **730**, 114 (2011).

[30]M. Wan, W. Matthaeus, H. Karimabadi, V. Roytershteyn, M. Shay, P. Wu, W. Daughton, B. Loring, and S. C. Chapman, "Intermittent dissipation at kinetic scales in collisionless plasma turbulence," Physical review letters **109**, 195001 (2012).

[31]H. Karimabadi, V. Roytershteyn, M. Wan, W. Matthaeus, W. Daughton, P. Wu, M. Shay, B. Loring, J. Borovsky, E. Leonardis, *et al.*, "Coherent structures, intermittent turbulence, and dissipation in high-temperature plasmas," Physics of Plasmas (1994-present) **20**, 012303 (2013).

[32]A. Bret and M. E. Dieckmann, "How large can the electron to proton mass ratio be in particle-in-cell simulations of unstable systems?" Physics of Plasmas (1994-present) **17**, 032109 (2010).

[33]M. Innocenti, G. Lapenta, S. Markidis, A. Beck, and A. Vapirev, "A multi level multi domain method for particle in cell plasma simulations," Journal of Computational Physics **238**, 115 – 140 (2013).

[34]A. Beck, M. Innocenti, G. Lapenta, and S. Markidis, "Multi-level multi-domain algorithm implementation for two-dimensional multiscale particle in cell simulations," Journal of Computational Physics **271**, 430 – 443 (2014), frontiers in Computational Physics Modeling the Earth System.

[35]M. Innocenti, A. Beck, T. Ponweiser, S. Markidis, and G. Lapenta, "Introduction of temporal sub-stepping in the multi-level multi-domain semi-implicit particle-in-cell code parsek2d-mlmd," Computer Physics Communications **189**, 47 – 59 (2015).

[36]W. Daughton, "Electromagnetic properties of the lower-hybrid drift instability in a thin current sheet," Physics of Plasmas (1994-present) **10**, 3103–3119 (2003).

[37]P. Pritchett, "Particle-in-cell simulations of magnetosphere electrodynamics," Plasma Science, IEEE Transactions on **28**, 1976–1990 (2000).

[38]S. P. Gary, *Theory of space plasma microinstabilities* (Cambridge university press, 2005).

[39]R. J. Goldston and P. H. Rutherford, *Introduction to plasma physics* (CRC Press, 1995).

[40]R. Davidson and N. Gladd, "Anomalous transport properties associated with the lower-hybrid-drift instability," Physics of Fluids (1958-1988) **18**, 1327–1335 (1975).

[41]R. Davidson, N. Gladd, C. Wu, and J. Huba, "Effects of finite plasma beta on the lower-hybrid-drift instability," Physics of Fluids (1958-1988) **20**, 301–310 (1977).

[42]E. Harris, "On a plasma sheath separating regions of oppositely directed magnetic field," Il Nuovo Cimento (1955-1965) **23**, 115–121 (1962).

[43]M. Ozaki, T. Sato, R. Horiuchi, *et al.*, "Electromagnetic instability and anomalous resistivity in a magnetic neutral sheet," Physics of Plasmas (1994-present) **3**, 2265–2274 (1996).

[44]P. Pritchett, F. Coroniti, and V. Decyk, "Three-dimensional stability of thin quasi-neutral current sheets," Journal of Geophysical Research: Space Physics (1978–2012) **101**, 27413–27429 (1996).

[45]G. Lapenta and J. Brackbill, "A kinetic theory for the drift-kink instability," Journal of Geophysical Research: Space Physics (1978–2012) **102**, 27099–27108 (1997).

[46]W. Daughton, "Kinetic theory of the drift kink instability in a current sheet," Journal of Geophysical Research: Space Physics (1978–2012) **103**, 29429–29443 (1998).

[47]R. Horiuchi and T. Sato, "Three-dimensional particle simulation of plasma instabilities and collisionless reconnection in a current sheet," Physics of Plasmas (1994-present) **6**, 4565–4574 (1999).

[48]G. Lapenta and J. Brackbill, "Nonlinear evolution of the lower hybrid drift instability: Current sheet thinning and kinking," Physics of Plasmas (1994-present) **9**, 1544–1554 (2002).

[49]H. Karimabadi, W. Daughton, P. Pritchett, and D. Krauss-Varban, "Ion-ion kink instability in the magnetotail: 1. linear theory," Journal of Geophysical Research: Space Physics (1978–2012) **108** (2003).

[50]H. Karimabadi, P. Pritchett, W. Daughton, and D. Krauss-Varban, "Ion-ion kink instability in the magnetotail: 2. three-dimensional full particle and hybrid simulations and comparison with observations," Journal of Geophysical Research: Space Physics (1978–2012) **108** (2003).

[51]X. Y. Wang, Y. Lin, L. Chen, and Z. Lin, "A particle simulation of current sheet instabilities under finite guide field," Physics of Plasmas **15**, 072103 (2008), http://dx.doi.org/10.1063/1.2938732.

[52]J. Brackbill, D. Forslund, K. Quest, and D. Winske, "Nonlinear evolution of the lower-hybrid drift instability," Physics of Fluids (1958-1988) **27**, 2682–2693 (1984).

[53]I. Silin, J. Büchner, and A. Vaivads, "Anomalous resistivity due to nonlinear lower-hybrid drift waves," Physics of Plasmas (1994-present) **12**, 062902 (2005).

[54]J. Büchner and W. Daughton, "Role of current-aligned instabilities in reconnection," in *Reconnection of Magnetic Fields: Magnetohydrodynamics, Collisionless Theory and Ob-*

servations (Cambridge University Press, 2007) pp. 144–153.

[55]M. E. Innocenti and G. Lapenta, "Momentum creation by drift instabilities in space and laboratory plasmas," Plasma Physics and Controlled Fusion **49**, B521 (2007).

[56]J. Büchner and N. Elkina, "Vlasov code simulation of anomalous resistivity," Space science reviews **121**, 237–252 (2005).

[57]W. Daughton, G. Lapenta, and P. Ricci, "Nonlinear evolution of the lower-hybrid drift instability in a current sheet," Physical review letters **93**, 105004 (2004).

[58]A. Divin, Y. V. Khotyaintsev, A. Vaivads, M. André, S. Markidis, and G. Lapenta, "Evolution of the lower hybrid drift instability at reconnection jet front," Journal of Geophysical Research: Space Physics (2015).

[59]J. Vranjes and S. Poedts, "Electric fields in solar magnetic structures due to gradient-driven instabilities: heating and acceleration of particles," Monthly Notices of the Royal Astronomical Society **400**, 2147–2152 (2009).

[60]I. Shinohara, T. Nagai, M. Fujimoto, T. Terasawa, T. Mukai, K. Tsuruda, and T. Yamamoto, "Low-frequency electromagnetic turbulence observed near the substorm onset site," Journal of Geophysical Research: Space Physics (1978–2012) **103**, 20365–20388 (1998).

[61]M. Øieroset, R. Lin, T. Phan, D. Larson, and S. Bale, "Evidence for electron acceleration up to 300 k e v in the magnetic reconnection diffusion region of earth's magnetotail," Physical Review Letters **89**, 195001 (2002).

[62]C. Cattell, J. Dombeck, J. Wygant, J. Drake, M. Swisdak, M. Goldstein, W. Keith, A. Fazakerley, M. André, E. Lucek, *et al.*, "Cluster observations of electron holes in association with magnetotail reconnection and comparison to simulations," Journal of Geophysical Research: Space Physics (1978–2012) **110** (2005).

[63]M. Zhou, X. Deng, S. Li, Y. Pang, A. Vaivads, H. Rème, E. Lucek, S. Fu, X. Lin, Z. Yuan, *et al.*, "Observation of waves near lower hybrid frequency in the reconnection region with thin current sheet," Journal of Geophysical Research: Space Physics (1978–2012) **114** (2009).

[64]C. Cattell, J. Wygant, F. Mozer, T. Okada, K. Tsuruda, S. Kokubun, and T. Yamamoto, "Isee 1 and geotail observations of low-frequency waves at the magnetopause," Journal of Geophysical Research: Space Physics (1978–2012) **100**, 11823–11829 (1995).

[65]S. Bale, F. Mozer, and T. Phan, "Observation of lower hybrid drift instability in the diffusion region at a reconnecting magnetopause," Geophysical research letters **29**, 33–1 (2002).

[66]A. Vaivads, M. André, S. Buchert, J.-E. Wahlund, A. Fazakerley, and N. Cornilleau-Wehrlin, "Cluster observations of lower hybrid turbulence within thin layers at the magnetopause," Geophysical research letters **31** (2004).

[67]T. Carter, H. Ji, F. Trintchouk, M. Yamada, and R. Kulsrud, "Measurement of lower-hybrid drift turbulence in a reconnecting current sheet," Physical review letters **88**, 015001 (2001).

[68]C. Escoubet, M. Fehringer, and M. Goldstein, "Introduction the cluster mission," in *Annales Geophysicae*, Vol. 19 (2001) pp. 1197–1200.

[69]L. Franci, S. Landi, L. Matteini, A. Verdini, and P. Hellinger, "High-resolution hybrid simulations of kinetic plasma turbulence at proton scales," arXiv preprint arXiv:1506.05999 (2015).

[70]K. Fujimoto and R. D. Sydora, "Electromagnetic particle-in-cell simulations on magnetic reconnection with adaptive mesh refinement," Computer Physics Communications **178**, 915–923 (2008).

[71]J.-L. Vay, P. Colella, A. Friedman, D. Grote, P. McCorquodale, and D. Serafini, "Implementations of mesh refinement schemes for particle-in-cell plasma simulations," Computer physics communications **164**, 297–305 (2004).

[72]M. E. Innocenti, M. Goldman, D. Newman, S. Markidis, and G. Lapenta, "Evidence of magnetic field switch-off in collisionless magnetic reconnection," The Astrophysical Journal Letters **810**, L19 (2015).

[73]H. Vu and J. Brackbill, "Celest1d: an implicit, fully kinetic model for low-frequency, electromagnetic plasma simulation," Computer physics communications **69**, 253–276 (1992).

[74]W. Daughton, J. Scudder, and H. Karimabadi, "Fully kinetic simulations of undriven magnetic reconnection with open boundary conditions," Physics of Plasmas **13**, 072101 (2006).

[75]L.-J. Chen, W. S. Daughton, B. Lefebvre, and R. B. Torbert, "The inversion layer of electric fields and electron phase-space-hole structure during two-dimensional collisionless magnetic reconnection," Physics of Plasmas (1994-present) **18**, 012904 (2011).

[76]H. Karimabadi, W. Daughton, and J. Scudder, "Multi-scale structure of the electron diffusion region," Geophysical Research Letters **34**, n/a–n/a (2007).

[77]M. A. Shay, J. F. Drake, and M. Swisdak, "Two-scale structure of the electron dissipation region during collisionless magnetic reconnection," Phys. Rev. Lett. **99**, 155002 (2007).

[78]J. F. Drake, M. A. Shay, and M. Swisdak, "The hall fields and fast magnetic reconnection," Physics of Plasmas (1994-present) **15**, 042306 (2008).

[79]Leibniz-Supercomputing-Centre, "`https://www.lrz.de/services/compute/supermuc/systemdescription/`,".

[80]M. Innocenti, A. Beck, S. Markidis, and G. Lapenta, "Momentum conservation in multi-level multi-domain (mlmd) simulations," Journal of Computational Physics **312**, 14–18 (2016).

[81]P. Ricci, J. U. Brackbill, W. Daughton, and G. Lapenta, "Influence of the lower hybrid drift instability on the onset of magnetic reconnection," Physics of Plasmas **11**, 4489–4500 (2004).

[82]P. Ricci, J. Brackbill, W. Daughton, and G. Lapenta, "New role of the lower-hybrid drift instability in the magnetic reconnectiona)," Physics of Plasmas (1994-present) **12**, 055901 (2005).

[83]G. Lapenta, S. Markidis, A. Divin, D. Newman, and M. Goldman, "Separatrices: The crux of reconnection," Journal of Plasma Physics **81**, 325810109 (2015).

[84]C. K. Birdsall and A. B. Langdon, *Plasma physics via computer simulation* (Taylor & Francis, 2004).

[85]J. P. Verboncoeur, "Particle simulation of plasmas: review and advances," Plasma Physics and Controlled Fusion **47**, A231 (2005).

[86]M. Drouin, L. Gremillet, J.-C. Adam, and A. Heron, "Particle-in-cell modeling of relativistic laser - plasma interaction with the adjustable-damping, direct implicit method," Journal of Computational Physics **229**, 4781 – 4812 (2010).

[87]B. Cohen, A. Langdon, D. Hewett, and R. Procassini, "Performance and optimization of direct implicit particle simulation," Journal of Computational Physics **81**, 151–168 (1989).

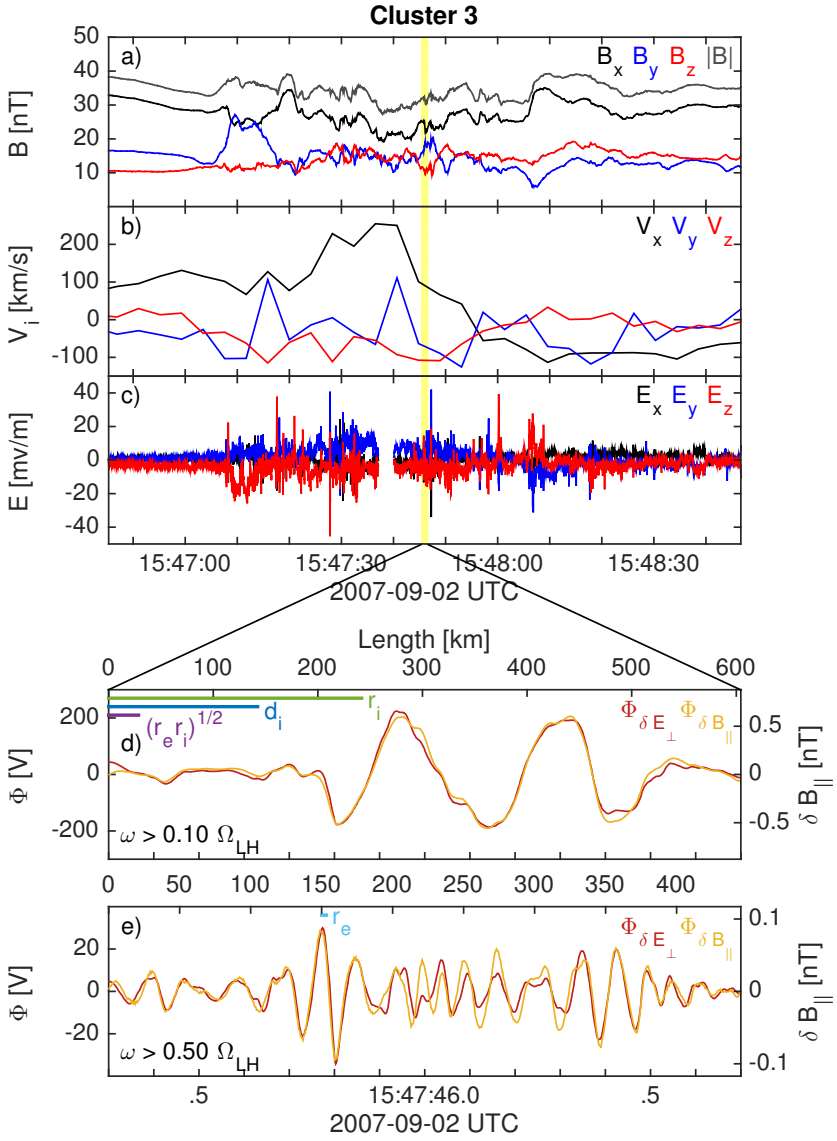

FIG. 16. Lower hybrid waves observed by Cluster 3 in the plasma sheet boundary layer. (a) Magnetic field. (b) Ion velocity. (c) Electric field. (d-e) The electrostatic potential obtained independently from the electric field and the magnetic field, respectively. The magnetic field strength is shown on the right hand axis. The fields are highpass filtered at (d) $0.1\Omega_{LH}$ (giving $\mathbf{v}_{ph} = 430\times[0.61\ \ -0.41\ \ -0.68]_{GSM}$ km/s) and (e) $0.5\Omega_{LH}$ (giving $\mathbf{v}_{ph} = 320\times[0.63\ \ -0.48\ \ -0.61]_{GSM}$ km/s) in order to seperate different length scales, which are shown on top of respective panel. For reference, d_i, r_i, $\sqrt{r_e r_i}$, and r_e are depicted in either panel.

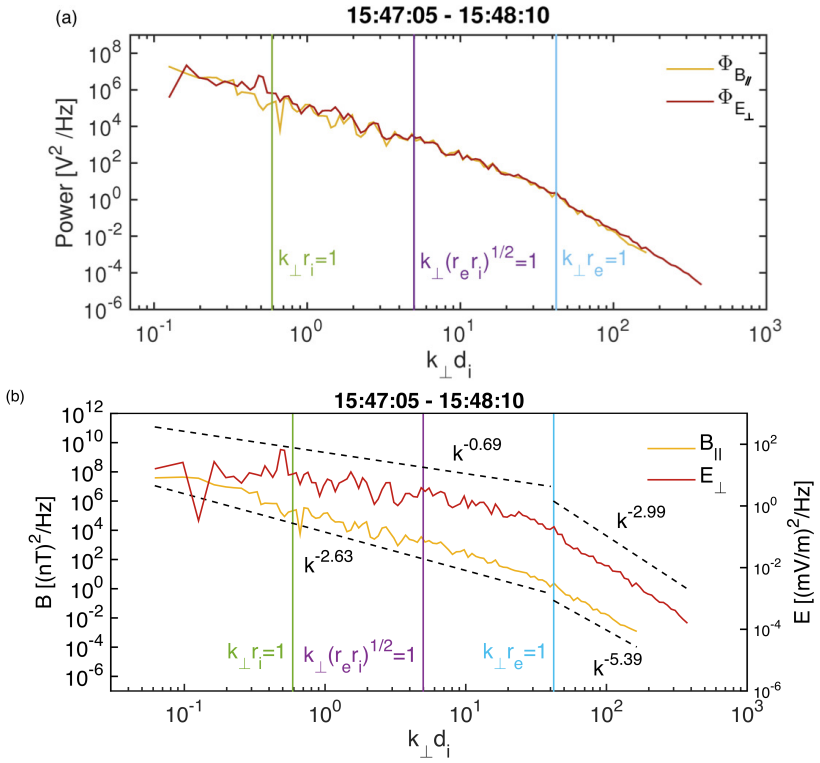

FIG. 17. Power spectra of $\Phi_{B_\parallel}$ (orange) and $\Phi_{E_\perp}$ (red) (panel a) and of the $B_\parallel$ (orange, left axis) and $E_\perp$ (red, right axis) (panel b) as a function of $k_\perp d_i$, calculated for the time interval $15:47:05-15:48:10$. The green, purple and light blue lines mark $k_\perp r_i = 1$, $k_\perp \sqrt{r_e r_i} = 1$ $k_\perp r_e = 1$, respectively. The calculated slopes for the spectra are superimposed in panel b.

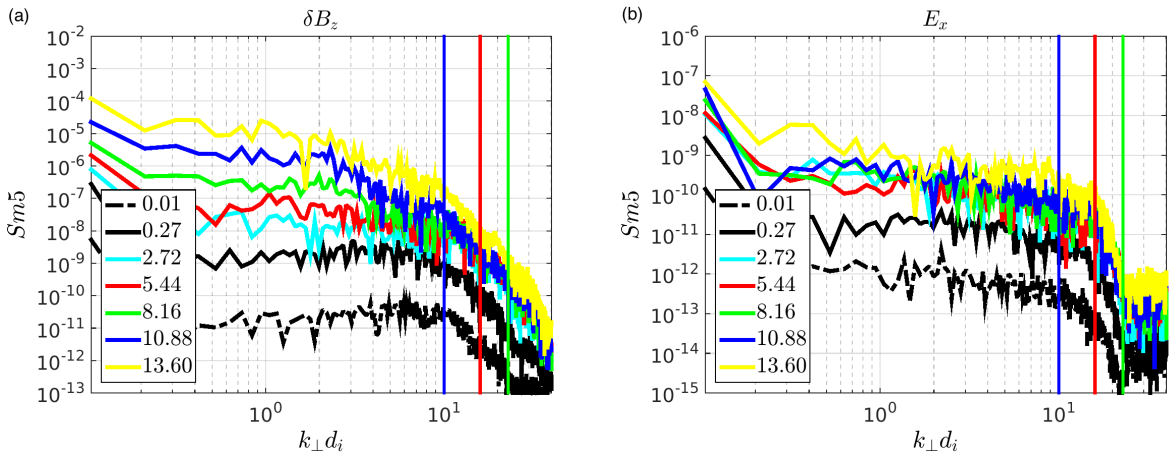

FIG. A18. Numerical power spectra of the fluctuations of the B_z (δB_z, top panel) and of the E_x (bottom panel) field components as a function of $k_\perp$, oriented at $\theta = 45°$ in the k_x vs. k_y plane, at the times $\Omega_{ci}t = 0.272$ (black line), $\Omega_{ci}t = 2.72$ (cyan), $\Omega_{ci}t = 5.44$ (red), $\Omega_{ci}t = 8.16$ (green), $\Omega_{ci}t = 10.88$ (blue) and $\Omega_{ci}t = 13.6$ (yellow). A smoothing level $Sm = 5$ is used in this simulation. The blue, red and green vertical lines at $k_\perp d_i = 10$, $k_\perp d_i = 16$ and $k_\perp d_i = 23$ mark the occurrence of structures in the δB_z and E_x power spectra. The black dash-dotted lines are the spectral values at a time, $\Omega_{ci}t = 0.01$, prior to the development of the different instabilities i.e. they can be used to assess noise levels.

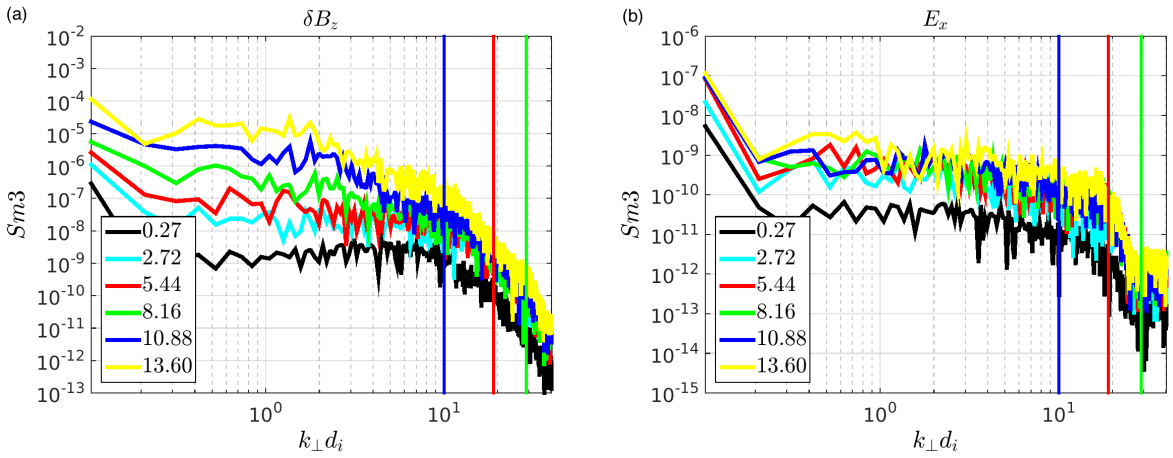

FIG. A19. Numerical power spectra of the fluctuations of the B_z (δB_z, top panel) and of the E_x (bottom panel) field components as a function of $k_\perp$, oriented at $\theta = 45°$ in the k_x vs. k_y plane, at the times $\Omega_{ci}t = 0.272$ (black line), $\Omega_{ci}t = 2.72$ (cyan), $\Omega_{ci}t = 5.44$ (red), $\Omega_{ci}t = 8.16$ (green), $\Omega_{ci}t = 10.88$ (blue) and $\Omega_{ci}t = 13.6$ (yellow). A smoothing level $Sm = 3$ is used in this simulation. The blue, red and green vertical lines at $k_\perp d_i = 10$, $k_\perp d_i = 19$ and $k_\perp d_i = 29$ mark the occurrence of structures in the δB_z and E_x power spectra.

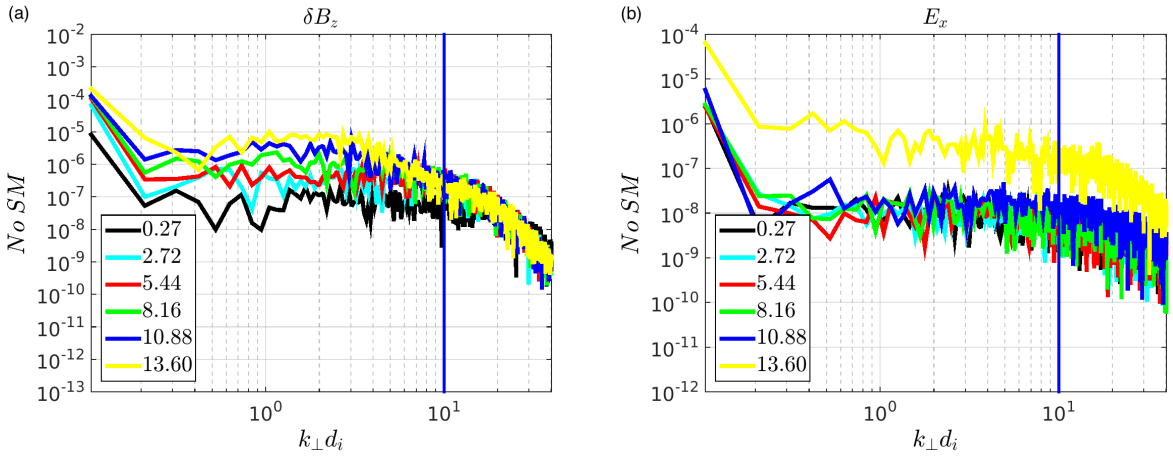

FIG. A20. Numerical power spectra of the fluctuations of the B_z (δB_z, top panel) and of the E_x (bottom panel) field components as a function of $k_\perp$, oriented at $\theta = 45°$ in the k_x vs. k_y plane, at the times $\Omega_{ci}t = 0.272$ (black line), $\Omega_{ci}t = 2.72$ (cyan), $\Omega_{ci}t = 5.44$ (red), $\Omega_{ci}t = 8.16$ (green), $\Omega_{ci}t = 10.88$ (blue) and $\Omega_{ci}t = 13.6$ (yellow). No smoothing is used in this simulation. The blue vertical lines at $k_\perp d_i = 10$ marks the occurrence of a structure in the δB_z power spectra.